AD-A113 674 UNITED TECHNOLOGIES RESEARCH CENTER EAST HARTFORD CT F/G 11/6
A STUDY OF THE DEPENDENCE OF MICROSEGREGATION ON CRITICAL SOLID--ETC(U)
JAN 82 D B SNOW, L E GREENWALD, E M BREINAN N00014-79-C-0649
UNCLASSIFIED UTRC/R82-914763-6 NL

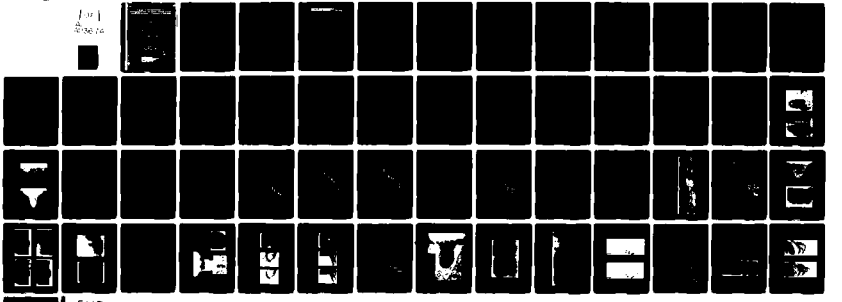

END
DATE FILMED
5-82
DTIC

A STUDY OF THE DEPENDENCE OF SOLIDIFICATION ON CRITICAL SOLIDIFICATION PARAMETERS IN RAPIDLY-QUENCHED STRUCTURES

Prepared by
D.B. Snow
L.E. Greenwald
E.M. Breinan

AD A113674

ANNUAL TECHNICAL REPORT

Contract N00014-79-C-0649
Project No. NR 031-825/5-15-80 (471)

for

Office of Naval Research
Department of the Navy
Arlington, Virginia 22217

DTIC
SELECTE
APR 20 1982
S D
A

by

East Hartford, Connecticut 06108

This document has been approved for public release and sale; its distribution is unlimited.

82 04 05 021

UNCLASSIFIED

SECURITY CLASSIFICATION OF THIS PAGE (When Data Entered)

REPORT DOCUMENTATION PAGE		READ INSTRUCTIONS BEFORE COMPLETING FORM
1. REPORT NUMBER R82-914763-6	2. GOVT ACCESSION NO. AD-A113 674	3. RECIPIENT'S CATALOG NUMBER
4. TITLE (and Subtitle) A STUDY OF THE DEPENDENCE OF MICROSEGREGATION ON CRITICAL SOLIDIFICATION PARAMETERS IN RAPIDLY-QUENCHED STRUCTURES		5. TYPE OF REPORT & PERIOD COVERED Annual Technical Report Aug. 1980 - Sept. 1981 6. PERFORMING ORG. REPORT NUMBER
7. AUTHOR(s) D. B. Snow, L. E. Greenwald, E. M. Breinan		8. CONTRACT OR GRANT NUMBER(s) N00014-79-C-0649
9. PERFORMING ORGANIZATION NAME AND ADDRESS United Technologies Research Center East Hartford, CT 06108		10. PROGRAM ELEMENT, PROJECT, TASK AREA & WORK UNIT NUMBERS
11. CONTROLLING OFFICE NAME AND ADDRESS Office of Naval Research Department of the Navy Arlington, VA 22217		12. REPORT DATE January 1982 13. NUMBER OF PAGES 50
14. MONITORING AGENCY NAME & ADDRESS(if different from Controlling Office)		15. SECURITY CLASS. (of this report) UNCLASSIFIED 15a. DECLASSIFICATION/DOWNGRADING SCHEDULE

16. DISTRIBUTION STATEMENT (of this Report)

Reproduction in whole or in part is permitted for any purpose of the United States Government

[illegible] approved [illegible] is unlimited.

17. DISTRIBUTION STATEMENT (of the abstract entered in Block 20, if different from Report)

18. SUPPLEMENTARY NOTES

19. KEY WORDS (Continue on reverse side if necessary and identify by block number)

Laser Welding
Laser Materials Processing
Fusion Zone Mixing
Deep Penetration Laser Welding
Shallow Penetration Laser Welding
Microsegregation
Critical Solidification Parameters
Rapidly Quenched Structures
Heat Transfer Calculations
Clad Alloy Welding

20. ABSTRACT (Continue on reverse side if necessary and identify by block number)

Grade AH32 structural hull steel clad with varying thicknesses of 317L stainless steel were bead-on-plate welded with a continuous, CO_2 laser operated at power settings of from 2 to 9 kW and scanned at 5 to 76 cm/sec. The resulting fusion zone shapes and microstructures were examined by light microscopy and electron microprobe to determine the variation in welding efficiency and fusion zone segregation as a function of beam power input and cladding

DD FORM 1 JAN 73 1473 EDITION OF 1 NOV 65 IS OBSOLETE
S/N 0102-LF-014-6601

UNCLASSIFIED

SECURITY CLASSIFICATION OF THIS PAGE (When Data Entered)

#20. Cont'd

thickness. Due to the similarity in thermal conductivity and reflectivity of the cladding and substrate, the degree of the dilution of chromium and nickel in the fusion zone depended only on the relative volumes of cladding and substrate mixed in it, and not the absolute values of cladding thickness or fusion zone depth. Welding efficiency increased with power and beam traverse speed at constant fusion zone depth. A region of inhomogeneous mixing characterized by a swirl-pattern microstructure was observed to extend from the bottom of the fusion zone wherever its depth exceeded the cladding thickness. The extent of this inhomogeneous region increased with increasing beam penetration below the cladding-substrate interface. Consequently, directed beam processing which attempts to preserve the composition of cladding or mix it homogeneously with the substrate should both avoid a deep-penetration fusion zone shape and minimize the depth of beam penetration into the substrate.

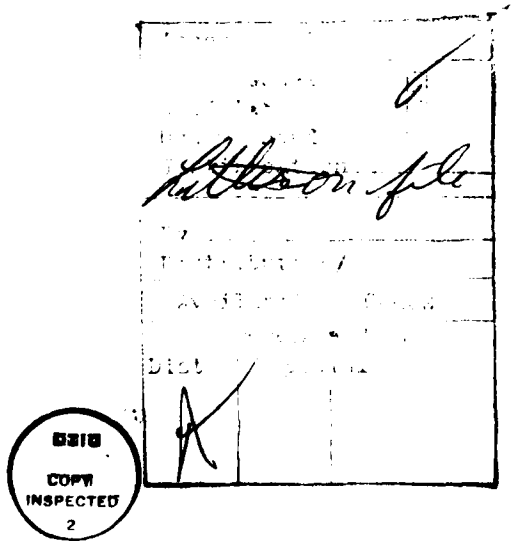

UNITED TECHNOLOGIES RESEARCH CENTER

UNITED TECHNOLOGIES

East Hartford, Connecticut 06108

R82-914763-6

A Study of the Dependence of Microstructure on Critical Solidification Parameters in Rapidly-Quenched Structures

ANNUAL TECHNICAL REPORT
N00014-79-C-0649

REPORTED BY D. B. Snow

L. E. Greenwald

E. M. Breinan

APPROVED BY E. R. Thompson, Manager of Materials Sciences

DATE Jan. 1982

NO. OF PAGES _____

COPY NO. _____

R82-914763-6

A Study of the Dependence of Microsegregation on Critical Solidification Parameters in Rapidly Quenched Structures

TABLE OF CONTENTS

A Study of the Dependence of Microsegregation on Critical Solidification Parameters in Rapidly Quenched Structures

I. INTRODUCTION

The laser processing of metals and alloys which have a preplaced surface layer of different composition has become the subject of increasing research activity in recent years, sufficiently so that comprehensive summaries of these efforts are contained in several recent papers on the technology of laser materials processing (Refs. 1-4). The materials to which this technique has been applied include such diverse alloy systems as chromium on iron (Ref. 4) and carbon steel (Refs. 2,3,5), hardfacing on a nickel base superalloy (Refs. 2,3,7) gold on nickel (Ref. 8), and copper-nickel on structural steel (Ref. 9). Additional examples of the application of laser cladding and laser surface alloying to other materials systems can be found in Ref. 2. Since the primary application of this type of laser processing is to alter the surface chemistry of a relatively inexpensive alloy in a cost effective and technologically useful way, it appeared appropriate to conduct a detailed examination of the homogeneity of mixing and the degree of alloy dilution produced by the cladding-substrate mixing in the fusion zone of a laser welded clad alloy is a function of laser power input. The results of this investigation will also be relevant to the cladding or surface alloying of metals by the LAYERGLAZE^{TM} process (Ref. 10).

II. EXPERIMENTAL PROCEDURE

A. Specimen Preparation

1. Material

The material selected for this study was structural hull steel, grade AH32 (ASTM A131), mechanically clad with type 371L stainless steel. All specimens were cut from a single plate of original dimensions 0.446" x 8" x 34" (1.13 cm x 20.3 cm x 86.4 cm) which was supplied by the Lukens Steel Company, Coatesville, PA. The compositions of the substrate steel and the stainless cladding layer are documented in Table I below.

Table I

Compositions of Starting Material

Base Plate ASTM A131 Lukens Heat No. B3649 (wt%)	Element	Stainless Cladding Type 317L Heat No. 17376 (wt%)
0.16	C	.016
1.37	Mn	1.73
0.005	P	0.027
0.014	S	0.004
0.21	Si	0.58
-	Ni	14.48
-	Cr	18.52
-	Mo	3.17
-	N	0.069

These compositions all fell within the range of acceptable specifications for the two alloys. The original thickness of the cladding material was 0.136" (0.345 cm) and the base metal 0.310" (0.787 cm).

2. Preparation of Specimens with Various Cladding Thicknesses

In order to provide a variety of cladding thicknesses, the plate was ground flat on the carbon steel face, and then the stainless cladding was reduced to the desired thickness by surface grinding. Melting tests were performed on 1" x 1" (2.54 cm x 2.54 cm) coupons. Although the task of adjusting the cladding

thickness by grinding prior to laser melting seems trivial, it was difficult to produce uniform thin clad layers at first. The original intent was to study the melting of layers which varied in thickness from 0.005" (0.013 cm) to 0.060" (0.152 cm). The thicknesses chosen were 0.005, 0.030, and 0.060" (0.013, 0.076, and 0.152 cm). Due to the difficulty of measuring the cladding thickness of the as-received plate, final dimensions achieved were 0.021, 0.055 and 0.080" (0.053, 0.140 and 0.203 cm). As a result, the matching of penetration to cladding thickness did not cover the full range desired. Subsequently, a second group of specimens was prepared with nominal premelting cladding thicknesses of 0.005, 0.010, 0.020 and 0.030" (0.013, 0.026, 0.051, and 0.076 cm). Although the machining of this series of specimens was carefully performed, there was a substantial, unexplained variation in the actual cladding thicknesses observed for these specimens during microstructural examination which followed both melting and metallographic sectioning. This direct measurement of cladding thickness is the most accurate one, and must be relied upon. The measured cladding thickness which was subjected to melting experiments, as compared to the target thicknesses, is tabluated in Table II. Given the way the specimens were prepared, there is no apparent explanation for this discrepancy, other than the possibility that the thickness of the original clad layer exhibited significant variation. This is believed to be unlikely, although it is noted that, as a result of the way the specimens were prepared, all variation in the original cladding thickness would show up entirely in the error portion of the final, as-reduced cladding thickness.

As a result of these variations in cladding thickness from the nominal values, the applied laser melting conditions (power density and speed) which were intended to either alloy or melt clad the bonded stainless layer to the underlaying ship plate were not always properly matched to the stainless layer thickness or intended depth of substrate penetration. Nevertheless, due to the large amount of experimental data taken, a sufficient variation of welding conditions was achieved so as to provide adequate data for the study, as reported herein. For any future work in the area, the importance of verifying the cladding layer thickness prior to laser melting should be stressed. The added cost of sectioning and preparing the samples prior to melting tests appears justified, because it is really the most direct and reliable technique for determining cladding coating thickness. In addition, due to the apparent inability to produce broad, flat-bottomed, "shallow penetration" melt zones to depths in excess of 0.025 cm, increased investigation of thinner clad layers, and their mixing with the substrate, would be of interest.

3. Laser Melting for Alloying and Cladding

Square specimens measuring 1" x 1" (2.54 cm x 2.54 cm) were provided for laser melting with a variety of bonded stainless cladding thicknesses, as indicated above. Since the underlying steel substrate thickness was greater than 0.3" (0.76 cm) all specimens were felt to closely approximate an infinite heat

Table II

Comparison of Nominal and Measured Cladding
Thicknesses of Specimens for Laser Melting Tests

Nominal Thickness (in.)	Nominal Thickness (cm)	Measured Thickness (in.)	Measured Thickness (cm)
.005	.013	.016-.019	.041-.048
.005	.013	.017-.018	.043-.046
.005	.013	.030-.036	.076-.091
.005	.013	.007-.008	.018-.020
.010	.025	.038-.039	.096-.099
.010	.025	.024-.026	.061-.066
.010	.025	.051-.055	.130-.140
.020	.051	.017-.020	.043-.051
.020	.051	.021-.024	.053-.061
.020	.051	.008-.013	.020-.033
.020	.051	.020	.051
.030	.076	.054	.137
.030	.076	.044-.054	.112-.137
.030	.076	.018-.020	.046-.051
.030	.076	.048-.051	.122-.130

sink for the melt depths investigated. Specimens were cleaned of any residual contamination after grinding by an acetone wash followed by an alcohol wash, and were placed in clean paper envelopes. Although the elapsed time between grinding and melting tests was not controlled, no oxidation problems which could influence the results of the melting tests were expected from the 317L cladding layer.

The actual melting was performed by mounting the specimens on a horizontal rotating wheel similar to that described in Ref. 11. The height of each specimen was adjusted so that the top of the stainless cladding layer lay in the focal plane of the laser beam, 18" (45.72 cm), below the focusing mirror. The beam was traversed across the specimen by rotating the wheel at various speeds, so that the trace of each fusion zone described an arc on each specimen surface with a radius of ~9" (22.9 cm). A photograph of the rotating wheel setup, including some sample mounting blocks located within the trough area appears in Fig. 1a. This wheel is flanged at its outer rim to create an integral trough. It is equipped with a labyrinth-sealed cover and an internal shielding gas distribution system in order to flood the trough with shielding gas for the purpose of protecting the hot, molten specimen surfaces from the atmosphere. As an added feature, the shielding gas may be used to control or influence the formation of an energy absorbing plasma above the workpiece surface. In the course of these experiments only pure helium, which results in minimal plasma formation, was used for shielding.

The laser utilized for these tests was a continuous, convectively-cooled, high power carbon dioxide laser operated in the unstable resonator mode at power settings from 2.0 to 9.0 kW. The power losses caused by absorption at mirrors as the beam passed along the external optical train were estimated at 4% per reflecting surface, so that power actually delivered at the workpiece was approximately 78% of the set power level. The diameter of the focused laser beam at the workpiece surface was estimated to be 0.030" (0.076 cm), so that the range of power densities actually impinging on the workpiece surface was 3.5×10^5 to 1.55×10^6 w/cm^2. Tables III and IV indicate the ranges of melting conditions which were applied to specimens with a variety of clad layer thicknesses in the course of this study.

Table III

Laser Melting Conditions
Alloying and Cladding - First Test Series

(The following matrix of speeds and powers was applied to specimens with clad layer thicknesses of 0.021" (0.053 cm), 0.055" (0.14 cm), and 0.080" (0.203 cm)

Laser Power, kW Set	Delivered	Scanning Speeds, cm/sec						
2.0	1.57	5.1	10.2	15.2	20.3	39.2	50.8	76.0
4.0	3.13	5.1	10.2	15.2	20.3	39.2	50.8	76.0
6.0	4.70	5.1	10.2	15.2	20.3	39.2	50.8	76.0
8.0	6.26	5.1	10.2	15.2	20.3	39.2	50.8	76.0
9.0	7.04	5.1	10.2	15.2	20.3	39.2	50.8	76.0

Table IV

Laser Melting Conditions
Alloying and Cladding - Second Test Series

(The following matrix of speeds and powers was applied to specimens with nominal clad layer thicknesses of 0.005" (0.013 cm), 0.010" (0.025 cm), 0.020" (0.051 cm) and 0.030" (0.076 cm). See above for a discussion of actual vs nominal clad thicknesses)

Laser Power, kW Set	Delivered	Scanning Speeds, cm/sec						
4.0	3.13	5.1	10.2	15.2	20.3	39.2	50.8	76.0
6.0	4.70	5.1	10.2	15.2	20.3	39.2	50.8	76.0
8.0	6.26	5.1	10.2	15.2	20.3	39.2	50.8	76.0
9.0	7.04	5.1	10.2	15.2	20.3	39.2	50.8	76.0

B. Microstructural Analysis

Both transverse and longitudinal cross sections of the fusion zone were examined by optical microscopy and scanning electron microscopy. The depth of penetration was determined from the average value measured from micrographs of three separate transverse cross sections of each specimen. Some of these transverse sections were also characterized by qualitative and quantitative X-ray analysis, including X-ray mapping, with Ni Kα, Fe Kα and Cr Kα signals utilizing a Cameca "CAMEBAX" scanning electron microprobe. An attempt was made to obtain similar microstructural and chemical data at higher resolution by STEM microanalysis, but the beam deflection and general image distortion caused by the interaction of the ferromagnetic specimens with the strongly activated objective lens of the Philips EM400T TEM/STEM proved to be too great to achieve this.

III. RESULTS AND DISCUSSION

A. Analysis of Weld Cross-Section Geometry

The purpose of this effort was to model several technologically important aspects of the laser welding of stainless-clad steel. Specifically, these were the heat transfer phenomena and the relationship of the resulting weld geometry to the basic welding parameters of beam intensity and speed. To establish a data base for this task, a large number of welds were made on 317L stainless-clad structural hull steel, ASTM A131, grade AH32, as described previously. It was found that the geometry of the fusion zone viewed in transverse cross section could be correlated with welding speed and beam intensity. In general, two types of weld cross-sections were formed, as shown in Fig. 2. The "bowl" shape of Fig. 2a was formed at the lower power levels and/or higher speeds. At certain combinations of speeds and powers, a deep penetration cone appeared at the bottom of the bowl (Fig. 2b). As the power was increased and/or the speed decreased, the cone penetrated more deeply. The shape of the fusion zone and the initiation of the deep penetration cone appeared to be independent of the clad thickness. This observation was anticipated because the thermal properties (conductivity, specific heat, etc.) of the stainless cladding and the steel substrate are similar. Further, it is reasonable to expect that this result can be generalized to other materials, i.e. penetration depths and fusion zone shapes from laser welds in a homogeneous material can be used to predict weld geometry in clad materials having similar thermal properties.

To aid in the subsequent discussion of melt patterns, a schematic of a typical weld cross section is shown in Fig. 3. The nomenclature of the schematic is as follows.

Abbreviations Used to Describe Fusion Zone Geometry
d_b = bowl depth, cm
d_t = total penetration depth, cm
W_b = bowl width, cm
W_c = maximum cone width, cm

The change in <u>shape</u> of the bowl-and-cone pattern was fairly consistent over the range of welding conditions, despite the irregularities and asymmetries that occurred from weld to weld. Figure 4 shows the schematic cross section of Fig. 3 with the outlines of actual welds superimposed to illustrate the repeatability of the geometry.

Measurements of total melt depth, d_t, are shown in Figs. 5, 6, 7 and 8 for input power levels of 1.57, 3.13, 4.70, and 6.26 kW, respectively. The data were taken from two groups, or runs, of welding passes. The groups are basically a repeat of the same powers and speeds but with different thicknesses of cladding. Open and closed symbols are used to differentiate measurements from the two groups.

Although there was some scatter, the data were sufficiently concentrated that fusion zone depth trend lines were obvious. The triangular symbols indicate individual measurements of total penetration depth, d_t, whether for a simple blow shape or a bowl plus a deep penetration cone; and the solid lines represent the trend of the total melt depth. The circular symbols indicate measurements of apparent bowl depth, d_b, whether or not an additional penetration cone had formed. The dashed lines represent the trend of bowl depth.

Figure 8 summarizes, on a linear scale, the fusion zone depth trends shown in Figs. 5-8. The circles are the points of deep penetration cone initiation from the bottom of the bowl. The locus of these break points is significant because it defines the combinations of beam power and welding speed at which melt depth increases rapidly with further small reductions in welding speed. The well-defined breaks in the curves are evidence of a dramatic change in the energy capture mode of the beam; a "keyhole" forms to permit transfer of energy to the material beneath the surface. The effect of this phenomena on welding efficiency is discussed at the end of this section.

The width of the melt region was also found to vary with beam power and welding speed as shown in Fig. 10. Measured data are indicated by symbols, and trends are shown by solid lines. Superimposed on the figure are the approximate beam diameter (at the workpiece) of 0.076 cm and the locus of breakpoints at which the deep penetration cone begins to occur. Note that the two lines are almost parallel and are quite close together. From this observation it appears that melt width is approximately equal to beam width at the initiation of deep penetration and that melt width increases with decreasing weld speed (for a constant power level).

The width of the base of the penetration cone is shown as a function of beam power and welding speed in Fig. 11. Measured data are indicated by symbols, and trends are shown by solid lines. Smoothly varying characteristics resulted as shown by the trend lines. No data are given for the 1.57 kW power level since no deep penetration occurred at that power level for the welding speeds considered.

1. Welding Efficiency

An analysis was performed to determine welding efficiency as a function of beam intensity and welding speed. Welding efficiency was defined as the percentage of energy in the incident beam that is utilized in melting the cladding and the substrate. The remainder of the incident energy is either (1) reflected from the surface of the material (or the surface plasma), (2) expended in the formation of vapor and plasma, or (3) conducted into the solid material both downward and outward from the molten weld zone. Using this definition of welding efficiency, it is seen that even if all of the incident energy of the beam were captured by the material (zero reflectance), the weld efficiency could approach, but never reach, 100% because of conduction losses. Welding efficiency will increase with an increasing rate of energy absorption (per unit cross sectional area of weld) because less time will be available for conduction losses during the melting process.

2. Deviation of Efficiency Equation

It was assumed that the cladding and the substrate material could be treated as a homogeneous medium undergoing heat transfer because of the similar thermal properties of the two materials. If the cross sectional area of the weld is A, then energy E_{melt} (joules), required to melt a length L of material is given by

$$E_{melt} = \rho AL \, [c_p \, (T-T_o) + h] \qquad (1)$$

where A = cross-sectional area of weld (cm^2)
c_p = specific heat (gm-°C)
h = heat of fusion (j/gm)
L = length of weld (cm)
T = bulk temperature of melt (°C)
T_o = initial temperature (°C)
ρ = density (gm/cm^3).

For simplicity, the material was assumed to be at a bulk (or average) temperature T which is above the melt temperature, T_{melt}.

If the speed of the beam is V cm/sec then the length L can be expressed as

$$L = V \, \Delta t \qquad (2)$$

where Δt (sec) is the time interval required to traverse the length L. The total energy, E_o (joules), incident on the surface from the beam in the time interval Δt is

$$E_o = P\ \Delta t \tag{3}$$

where P is the power in the beam (watts).

Substituting Eqs. (2) and (3) into Eq. (1), and defining efficiency as E_{melt}/E_o, yields an expression for the welding efficiency η:

$$\eta = \frac{E_{melt}}{E_o} = \frac{\rho AV}{P}\ [c_p\ (T-T_o) + h] \tag{4}$$

The effective welding efficiency η for all welds made in the stainless-clad ship plate can be calculated using Eq. (4). The welding parameters, P (power at the workpiece) and V (speed), are known and the material properties and temperatures are as given below.

Physical Constants	
c_p	= 0.5025 j/gm-°C
h	= 279 j/gm
T	= 2000°C
T_{melt}	= 1400°C
T_o	= 21.1°C

The bulk temperature, T, of the melt was assumed to be 2000°C (the vaporization temperature of the material is about 2700°C).

The cross-sectional area, A, of the weld was calculated using Fig. 3 as a model of the melt shape, and the trend lines from Figs. 5 through 11 for the dimensions of the individual bowl and cone shapes. The bowl portion was assumed to have the shape of a semi-ellipse and the cone to have the shape of a parabola. The total cross-sectional area is

$$A = A_{bowl} + A_{cone} \tag{5}$$

or

$$A = \frac{\pi}{2}\left(\frac{W_b}{2}\right) d_b + \frac{2}{3} W_e\ (d_t - d_b) \tag{6}$$

The cross-sectional area A can thus be determined from Eq. (6) and Figs. 5 through 11, and then substituted into Eq. (4) in order to calculate the welding efficiency as a function of weld power and speed. The results are shown as solid lines in Fig. 12, where the locus of the initiation of deep-penetration cones is also indicated.

For the lowest delivered power level of 1.57 kW, the weld efficiency, defined as the percentage of incident power that goes to form the fusion zone, is only about 2.5%. Here, no penetration cones were formed and melt width is less than the beam diameter (Fig. 10).

If Figs. 10 and 12 are correlated, it is found that when the melt width is equal to the beam diameter, the efficiency is nearly constant at 10%. The results are summarized below.

Power (kW)	Speed (cm/sec)	Efficiency (%)
6.26	64	10.5
4.70	43	10.0
3.13	17	9.4

It is interesting to note that the rapid increase in penetration depth below a threshold speed that was observed in Fig. 9 does not correspond to a similar (rapid) increase in welding efficiency as seen in Fig. 12. Welding efficiency is seen to increase as speed is decreased but there is not a large change in its rate of increase after the penetration cone begins to form. This can be explained by the fact that while total penetration depth increases rapidly, the resulting melt area increases slowly because of the relatively narrow width of the cone (compared to the bowl).

Maximum welding efficiency is seen to approach 40% at 6.26 kW delivered power and a 5 cm/sec welding speed; i.e., 40% of the incident energy has gone into melting the cladding and the substrate.

The dotted lines on Fig. 12 show the variation of welding efficiency for conditions of constant melt depth. It is apparent that for a constant melt depth, welding efficiency increases with increasing speed (and power). This effect is due to the fact that at higher welding speeds, less time is available for conduction heat loss to the surrounding material. Note the closeness of the line of 0.025 cm melt depth and the locus of penetration-cone initiation. From this observation it is apparent that laser cladding to a depth of greater than 0.025 cm will result in welds whose deepest penetration extends only over a portion of the total width of the weld.

For weld depths greater than 0.025 cm, a multiple-pass technique will be required to completely melt all of the material below the 0.025 cm depth. Because of the overlapping melt zones, the net efficiency of a deep welding process will be poor despite the relatively high efficiency of the individual welds; i.e. surface portions of the material are melted and remelted due to overlap.

B. Fusion Zone Microstructure

1. Longitudinal Section

Considerable variation was noted in the fusion zone depth of penetration as measured from three separate transverse cross sections of each individual weld. This did not appear to affect the mathematical analysis, as the average geometric parameters of the fusion zone varied quite systematically with power input. To examine this behavior more closely, several welds were sectioned longitudinally; that is, so that both the beam traverse and propagation directions lay in the plane of view. All of the welds which combined a deep-penetration fusion zone with a relatively slow beam traverse speed (<20 cm/s) exhibited the periodic variation in depth of penetration with distance shown in Fig. 13. Variation in the beam output energy did not appear to cause this phenomenon. It was monitored by calorimetry before and after this group of welds was made, and did not vary more than $\pm$3%. The Japanese, however, have observed that high energy, slow traverse rate electron beam welds in aluminum exhibit a similar periodic variation in depth of penetration (Ref. 14). They ascribe this behavior to oscillation in the gravity-driven mass flow of liquid metal down the walls of the vapor column surrounding the beam, and have recorded such behavior by motion pictures. It is probable that the same phenomenon occurred in this study, and that it can be suppressed by increasing or decreasing the beam traverse speed.

When the depth of fusion zone penetration changes substantially near the cladding-substrate interface, the homogeneity of mixing and the overall chemistry of the fusion zone will change along with it. The swirled pattern at the deepest points of the fusion zone in Fig. 13 shows that the turbulence of the liquid fusion zone has not had time to completely mix the Cr and Ni in the cladding with the carbon steel of the substrate. This is not necessarily an undesirable situation. As will be discussed subsequently, the chemical and microstructural homogeneity of the fusion zone increases substantially with decreasing distance from the top surface of all welds.

2. General Microstructure

Several microstructural features were common to the fusion zone of all welds. Intergranular cracking of the 317L stainless cladding was a widespread phenomenon, and occurred in all areas of a given fusion zone not substantially

diluted by mixing with the substrate. The cause of this behavior is unknown, and did not affect the characterization of fusion zone geometry and microstructure. It should be noted that most of the 300 series austenitic stainless steels such as 304, 310 and 316 have been successfully laser welded (Ref. 12).

The microstructure of the fusion zone of all welds was dendritic, and usually displayed a decrease in dendrite arm spacing with increasing distance from the surface. Figure 14 shows a 200X view along the center line of a transverse section of the weld shown in Fig. 13. Two intergranular cracks are visible, ~0.65 and 1 mm above the root of the weld, respectively. The dendrite primary arm spacing varies from ~2μm near the root of the fusion zone to ~6.5μm near its surface. Thus the solidification rate has decreased in this particular weld from ~5 x 10^4°C/s near the root to ~2 x 10^3°C/s near the surface, the last region to solidify. The swirl pattern of the microstructure at the bottom of the fusion zone shows that this region solidified before the surface-tension-induced turbulent flow of the liquid metal could mix and homogenize the Cr and Ni in the stainless cladding with the carbon steel substrate (Refs. 2,3,13). This phenomenon was observed to varying degrees whenever the fusion zone penetrated more than a few microns into the substrate, and will be described in more detail subsequently.

3. Quantitative Characterization of Fusion Zone Microstructure

Very shallow penetration of the fusion zone below the cladding-substrate interface produced, as might be expected, a very minimal degree of dilution of the stainless steel composition. This is illustrated by Figs. 15-18, which show the microstructure, general spatial distribution of Cr and Ni in selected regions, and quantitative variation of Cr and Ni along the center line of the fusion zone of such a weld, viewed in transverse section. A good example of the fusion zone cracking in the 317L stainless cladding observed in all welds is shown in Fig. 15b. Some cracks penetrate into the heat affected zone, but do not propagate very far. The overall distribution of Cr and Ni in the fusion zone as determined by Cr Kα mapping and quantitative X-ray analysis (Figs. 17 and 18) is that of the original cladding. The 20 wt% Cr content shown in Fig. 18 is 1.5% greater than indicated by chemical analysis (Table I), and is about the maximum error expected from the electron microprobe analytical procedures. Note that even in the case of this particular weld in which a minimum volume of substrate was mixed into the cladding, an examination of Figs. 16a and 16b reveals a detectable (but technologically insignificant) amount of inhomogeneous mixing at the bottom tip of fusion zone. Given the relatively rapid solidification rate which occurs at the root of most laser welds, this type of "frozen-in" microstructural and compositional inhomogeneity can be assumed to be present to some degree in any laser weld in which the fusion zone penetrates the substrate. The extent of this incompletely mixed region, however, can be so small as to have no apparent practical influence on mechanical properties or corrosion resistance in the upper region of the fusion zone, as is the case here (Figs. 15-18).

The foregoing argument implies that deeper penetration of the fusion zone into the substrate should produce a larger region in which solidification has occurred before turbulent mixing has homogenized the melt. This was observed to be the case in this investigation for all welds which penetrated the substrate to a depth of ≥0.5 mm (0.02"), and is exemplified by the data in Figs. 19-22, which show a transverse section view of a weld made in 2.03 mm (0.080") clad material at 6.26 kW delivered power and 5.1 cm/s traverse speed. Figure 19 illustrates the prominent swirl patterns in the root of the fusion zone indicative of incomplete mixing. Figures 20 and 21 confirm that this microstructural pattern is caused by large gradients in chemical composition. The quantitative analysis of Cr and Ni content with depth along the center line of the fusion zone presented in Fig. 22 reveals that these elements have a relatively homogeneous distribution in the upper two-thirds of the fusion zone, but have decreased in average concentration by about 1.5-2 wt%. Below the original cladding-substrate interface, the average Cr and Ni content falls to the range of 3-5 wt% for each.

With increasing volume of substrate in the fusion zone relative to the volume of stainless steel cladding, general dilution of the relatively homogeneous upper region is observed in addition to an increased volume of incomplete mixing. Figures 23-27 show the fusion zone of a weld made in a specimen with 0.53 mm (0.021") thick cladding at 6.26 kW delivered power and 5.1 cm/s traverse speed. In this case, the welding parameters were the same as in the case previously described (Figs. 19-22), but the cladding was substantially thinner. The principal effect of this change is, as expected, an overall dilution of the Cr and Ni contents throughout the fusion zone. From Fig. 27 it can be seen that homogeneous mixing has occurred to a relatively large depth, 2.4 mm below the fusion zone free surface, and that it is very complete throughout a distance which is large compared to the original cladding thickness (0.53 mm). Below 2.4 mm, large local variations in Cr and Ni content are superimposed on a general decline in the amount of these elements with depth, as one might anticipate from the optical microstructure and characteristic X-ray intensity maps (Figs. 23-26). From a technological viewpoint, the main effect of decreasing the cladding thickness was to lower the Cr content from its original value of 18.5 wt% to an average of 8.5 $\pm$1.5 wt% throughout the fusion zone including the free surface at its top, a value well below the 12 wt% required for stainless properties.

To evaluate an extreme case of fusion zone deep penetration in clad material, a specimen with a 1.36 mm (0.053") thick cladding welded at 7.05 kW delivered power and 5.1 cm/s traverse speed was examined. As shown by Figs. 28-30, a reasonably uniform Cr content of 11.5 $\pm$1 wt% Cr was maintained to a depth of about twice the original cladding thickness. Below this level, the region of inhomogeneous mixing began, characterized by an abrupt decrease in the amount of both Cr and Ni (Fig. 30). It is of interest to note, however, that detectable Cr and Ni at a level of ~1-2 wt% were present even at the root of this fusion zone, 5 mm (0.2") below the surface and 3.7 mm (0.15") below the original cladding substrate interface.

It can be concluded that the two principal factors which control the degree of homogeneity in the fusion zone of laser welded stainless-clad structural steel are the shape of the fusion zone cross section and the relative volumes of cladding vs substrate which are mixed in it. The rapid solidification rate ($\sim 10^4$ °C/s) near the liquid-solid boundary of the fusion zone interrupts the mixing action of the liquid turbulence and creates a region of gross chemical inhomogeneity characterized by a pronounced swirl pattern in the microstructure and by sharp gradients in composition. If the cross section of the fusion zone is bowl-shaped, this poorly mixed region will be confined to a narrow layer next to the heat affected zone. If, however, the beam energy is large enough to create a fusion zone with a deep penetration spike, a relatively large region will solidify which is both inhomogeneous and dilute. Similar observations of the influence of fusion zone shape on homogeneity have been reported in specimens of laser welded iron and carbon steel coated or plated with chromium (Refs. 2,3,5), and in laser welds of structural hull steel clad with a copper-nickel alloy (Ref. 9). As noted in earlier investigations (Ref. 3), successive multiple passes, which have the effect of increasing the time during which liquid-state mixing can proceed, should homogenize the fusion zone to a greater degree. On the other hand, the elapsed time before solidification in almost all the volume of fusion zones which were bowl-shaped and in the upper regions of those with deep penetration spikes was sufficient to achieve fusion zone homogeneity on a macroscopic scale (i.e., over distances $>>6.5\mu m$, the maximum interdendritic spacing observed in the 317L stainless steel).

In all cases, however, the quantitative X-ray analyses revealed that liquid-state turbulent mixing was sufficiently rapid throughout most of the fusion zone to dilute the composition of the cladding in proportion to the volume of the substrate which was incorporated in it, even in the area near the top of the weld. Thus the degree of cladding dilution in both the inhomogeneous and/or homogeneous regions of any fusion zone did not depend on the absolute values of the cladding thickness or the depth of the fusion zone itself.

IV. RESULTS/CONCLUSIONS

1. The melt patterns were of such an irregular geometry as to render a heat transfer analysis beyond the scope of the study. The typical pattern consisted of a shallow, bowl-shaped region having a width approximately equal to the beam diameter. For the higher power, low-speed welds, a narrow penetration cone extending downward appeared.

2. The variation of melt patterns with speed and power followed a regular pattern. A locus of critical speed and power points was identified beyond which reductions in speed, for constant power, produced a rapid increase in the depth of the penetration cone.

3. The overall melt-pattern shape and total melt depth was independent of the cladding thickness. The result was probably due to the similarity of the thermal properties of the cladding and the substrate.

4. For the beam diameter used (0.076 cm), all of the welds with total melt depths greater than about 0.025 cm exhibited a deep penetration cone.

5. An analysis of the efficiency of the welding process showed that welding efficiency increased for increasing power and speed if melt depth is held constant. For deep welds, most of the energy is absorbed in the shallow bowl region rather than in the penetration cone. Thus, repetitive (overlapping) passes to completely weld the deep portions of the material would be inefficient because of the melting and remelting of the overlapping bowl material.

6. Mixing of clad or alloying material and substrate material has been observed to be always incomplete in some region of the fusion zone, usually the root. However, the fusion zone can be considered to be completely mixed for practical purposes under conditions which produce a bowl shape without a deep penetration spike.

7. The primary mechanism for fusion zone mixing is turbulent mixing of the liquid. If a deep penetration spike is formed, this mechanism will not operate for sufficient time to homogenize a large region in the root of the weld. Thus, deep penetration laser weld through a cladding of different composition than that of the substrate will be very inhomogeneous on a scale of $\geq 10\mu m$ in their lower regions.

8. The degree of overall dilution or alternation of the cladding composition depends on the relative volume of substrate incorporated in the fusion zone, not the absolute cladding thickness.

9. Long dwell times (slower scanning speeds) in the liquid promote more complete mixing and greater homogeneity. Welds with deep penetrations will be the most poorly mixed, due to the need for mass transport over longer distances and the more rapid solidification which occurs at the zone at the root of deep welds.

10. In order to preserve the composition of a cladding alloy, the volume of the fusion zone which intercepts the substrate must be minimized for any given cladding thickness. Minimal penetration beneath the clad layer is obviously easier to achieve as the cladding thickness increases.

11. The degree of mixing, as seen by optical metallographic examination of polished and etched surfaces of the fusion zone correlates accurately with X-ray maps and quantitative microprobe scans.

REFERENCES

1. D. A. Belforte, "High Power Laser Surface Treatment", Society of Manufacturing Engineers Technical Paper IQ77-373, 1977.

2. D. S. Gnanamuthu, "Laser Surface Treatment", Applications of Lasers in Materials Processing, E. A. Metzbower, ed., American Society for Metals, Metals Park, Ohio, 1979, p 177.

3. D. S. Gnanamuthu, "Laser Surface Treatment", Optical Engineering, 19 783-792 (1980).

4. L. R. Hettche, E. A. Metzbower, J. D. Ayers, and P. G. Moore, "Laser Assisted Metalworking - A Technology in Transition", Naval Research Reviews, 33, No. 2, 4-47 (1981).

5. P. A. Molian, "Effect of Fusion Zone Shape on the Composition Uniformity of Laser Surface Alloyed Iron", Scripta Met., 16, 65-68 (1982).

6. L. S. Weinman, J. N. DeVault, and P. Moore, "Properties of Rapidly Solidified, Laser Surface Alloyed, Low Carbon Steels", Applications of Lasers in Materials Processing, E. A. Metzbower, ed., American Society for Metals, Metals Park, Ohio, 1979, p 245.

7. W. M. Steen and C. G. H. Courtney, "Hardfacing of Nimonic 75 Using 2 kW Continuous-Wave CO_2 Laser", Metals Tech., June 1980, p 232.

8. C. W. Draper and L. S. Meyer, "Laser Surface Alloying of Gold Films on Nickel", Applications of Surface Science, 7, 276-280 (1981).

9. C. M. Banas, "Laser Weld Attachment of Cu-Ni Alloy to Ship Steel", Final Report, International Copper Research Assn. (INCRA) Project 241, United Technologies Research Center, March 1981.

10. E. M. Breinan, D. B. Snow and C. O. Brown, "Program to Investigate Advanced Laser Processing of Materials", Final Report, DARPA Sponsorship, ONR Contract N00014-78-C-0387, January 1981.

11. E. M. Breinan, B. H. Kear, and C. M. Banas, "Processing Materials with Lasers", Physics Today, November 1976, pp 44-50.

12. R. A. Willgoss, J. H. P. C. Megaw, and J. N. Clark, "Assessing the Laser for Power Plant Welding", Source Book on Electron Beam and Laser Welding, M. M. Schwartz, ed., American Society for Metals, Metals Park, Ohio, 1981, p 341.

13. T. R. Anthony and H. E. Cline, "Surface Rippling Induced by Surface Tension Gradients During Laser Surface Melting and Alloying", JAP, 48, 3888-94 (1977).

14. Y. Arata, B. Abe and M. Fujisawa, "A Study on Dynamic Behavior of Electron Beam Welding by a Fluoroscopic Observation", Proc. 2nd International Symposium, Japan Welding Soc., Osaka, August 25-27, 1975.

COVERED WHEEL ASSEMBLY UTILIZED FOR LASER WELD CRACK TESTING

(a) MOVING PORTION OF ASSEMBLY WITH COVER REMOVED AND SIX SPECIMENS IN PLACE, 23 CM FROM WHEEL CENTER

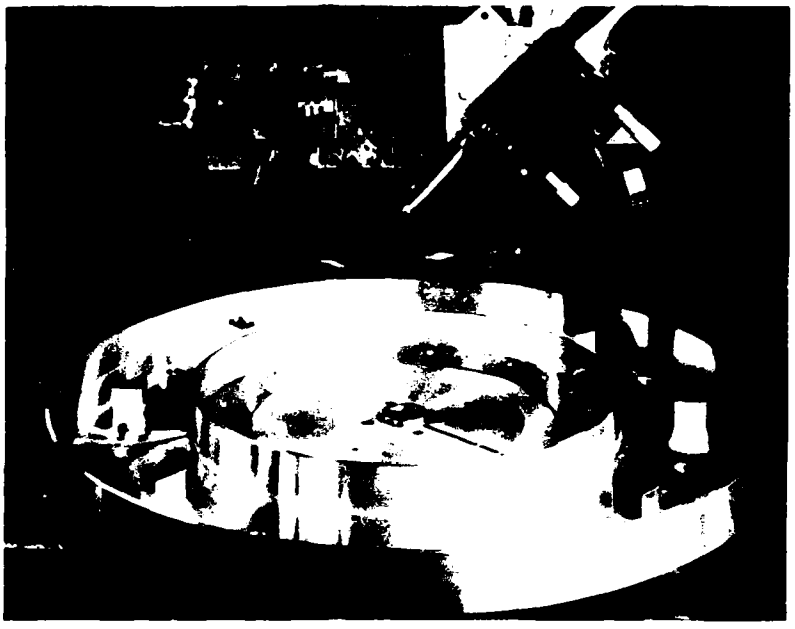

(b) STATIONARY COVER IN PLACE; LASER BEAM PORT AT 12 O'CLOCK

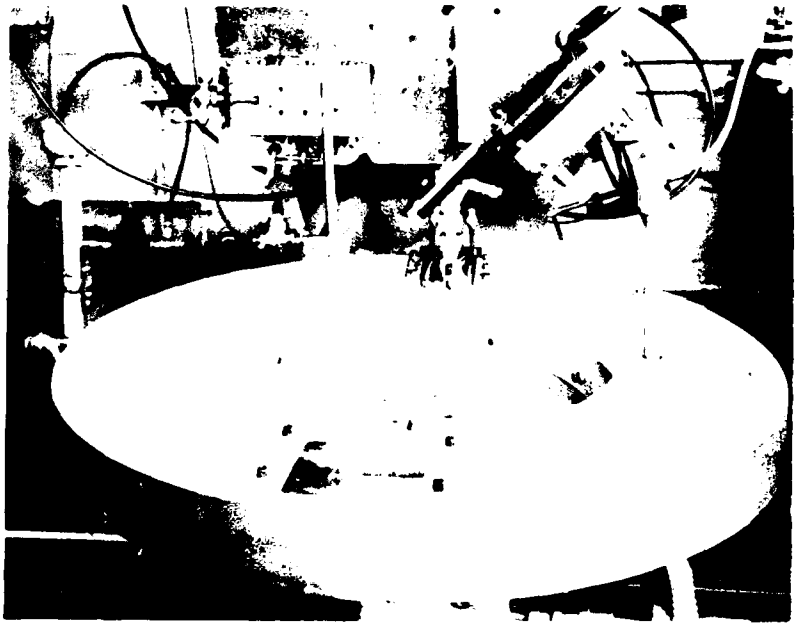

FIG. 2

TYPICAL MELT PROFILES

P = 3.13 kW

a) SPEED = 10.2 cm/sec

100μm

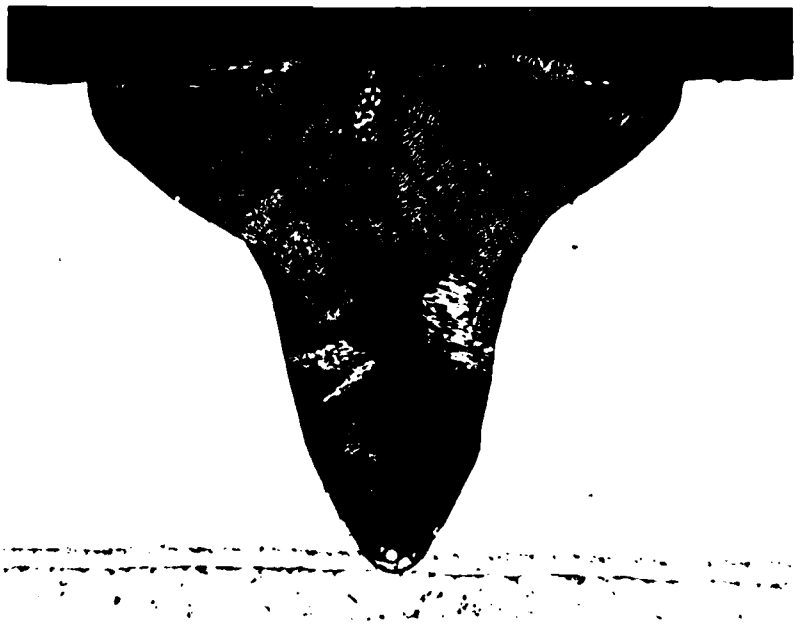

b) SPEED = 5.1 cm/sec

200μm

81-10-52-1

WELD CROSS-SECTION GEOMETRY

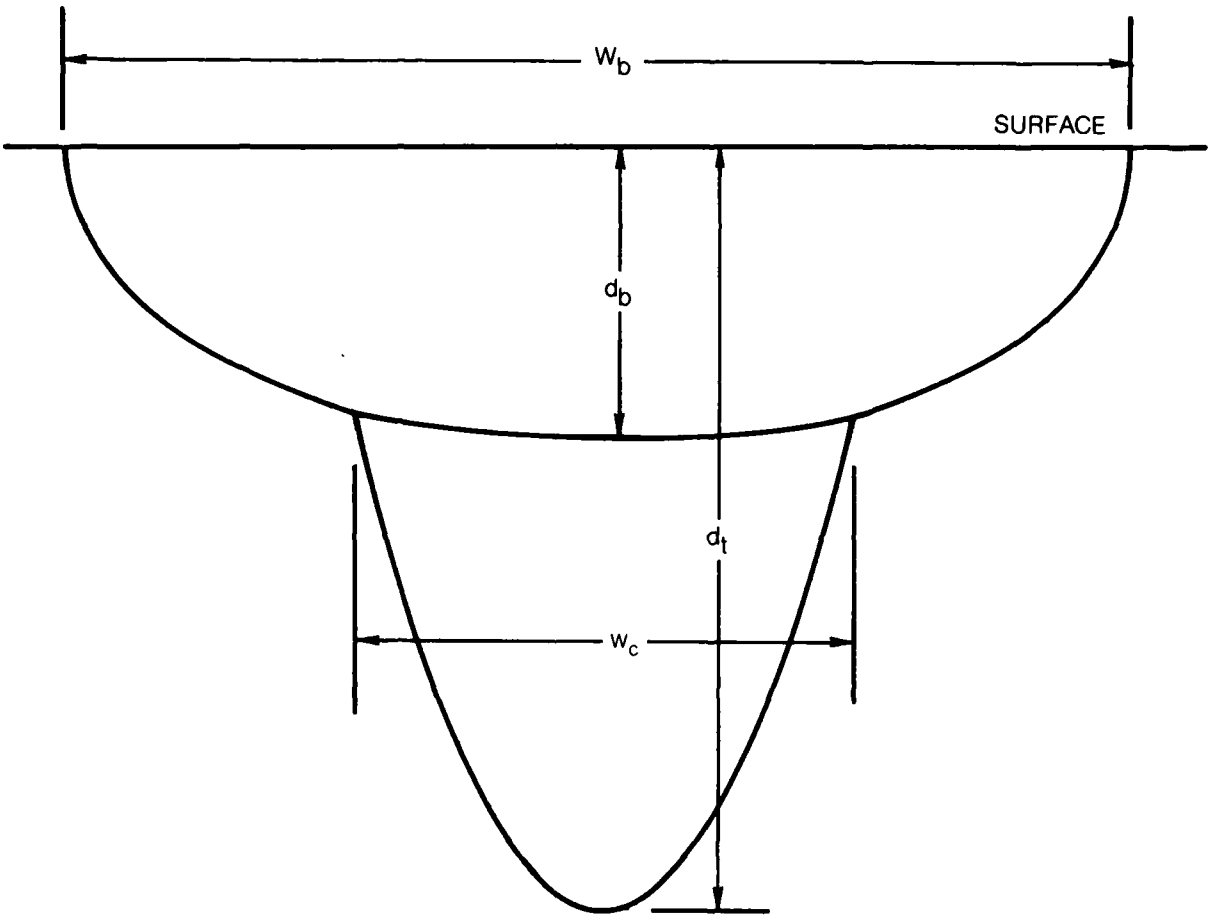

81-10-52-2

TYPICAL DEEP PENETRATION PATTERNS

POWER = 4.70 kW
SPEED = 5.1 cm/sec

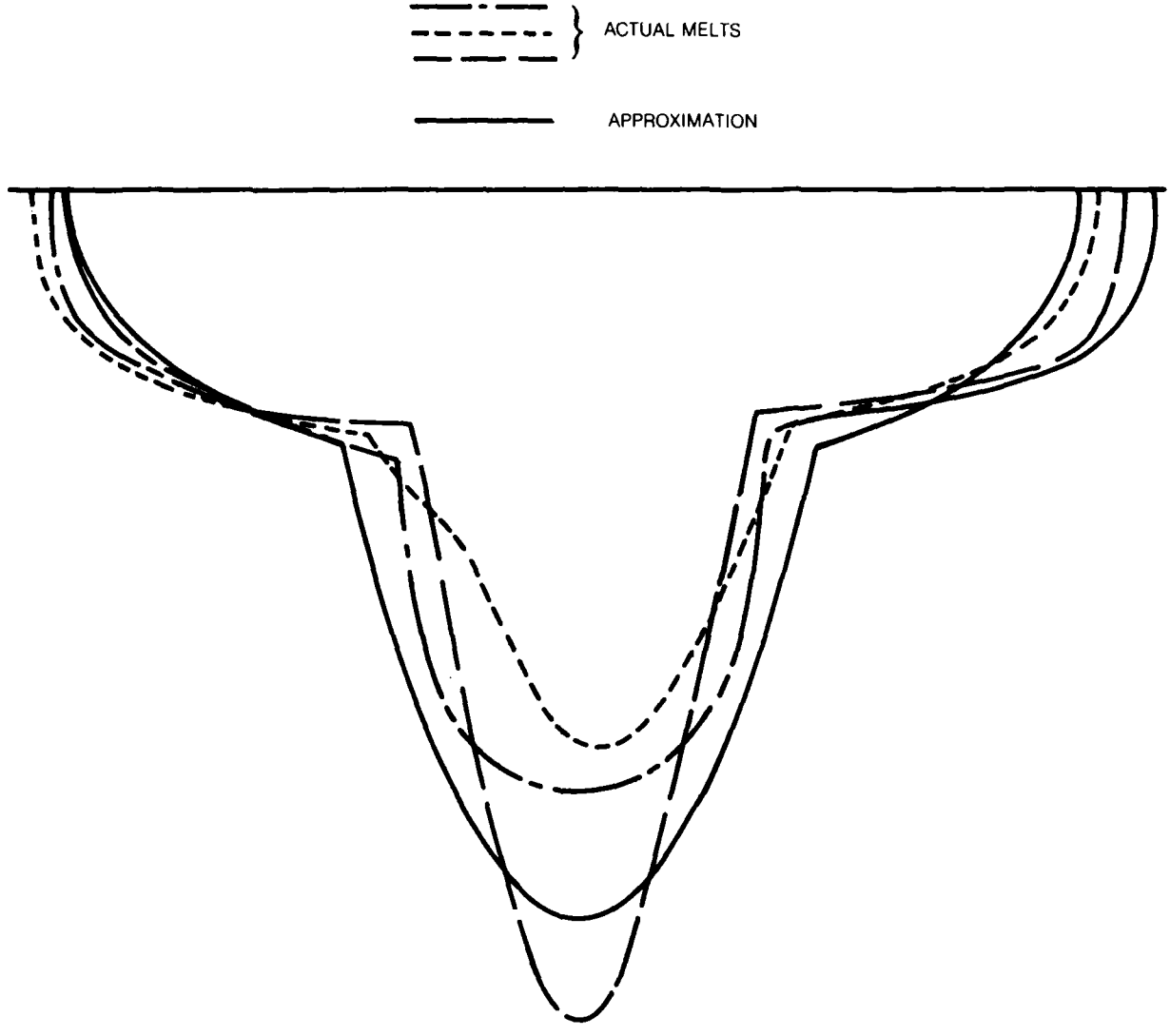

81-10-52-3

MELT DEPTH

1.57 kW
GROUP ONE ONLY

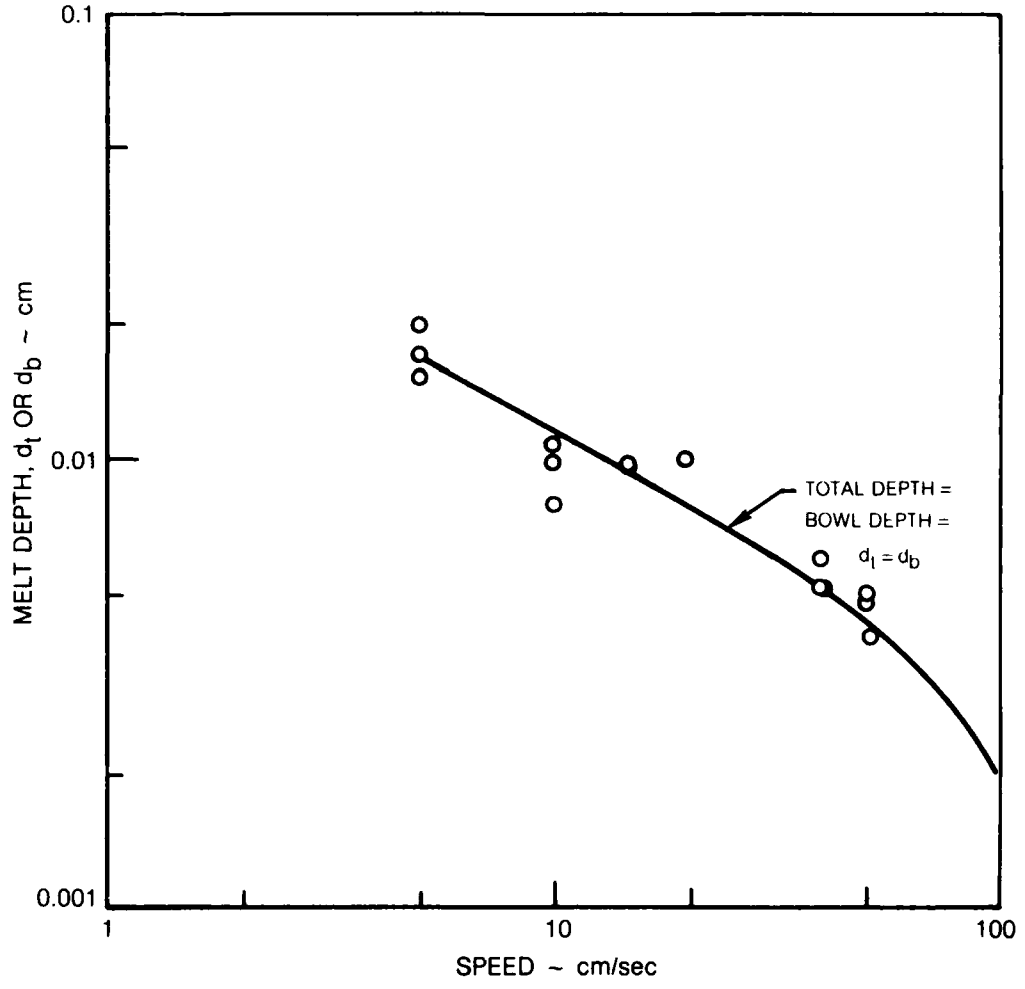

81-10-52-4

MELT DEPTH

3.13 kW

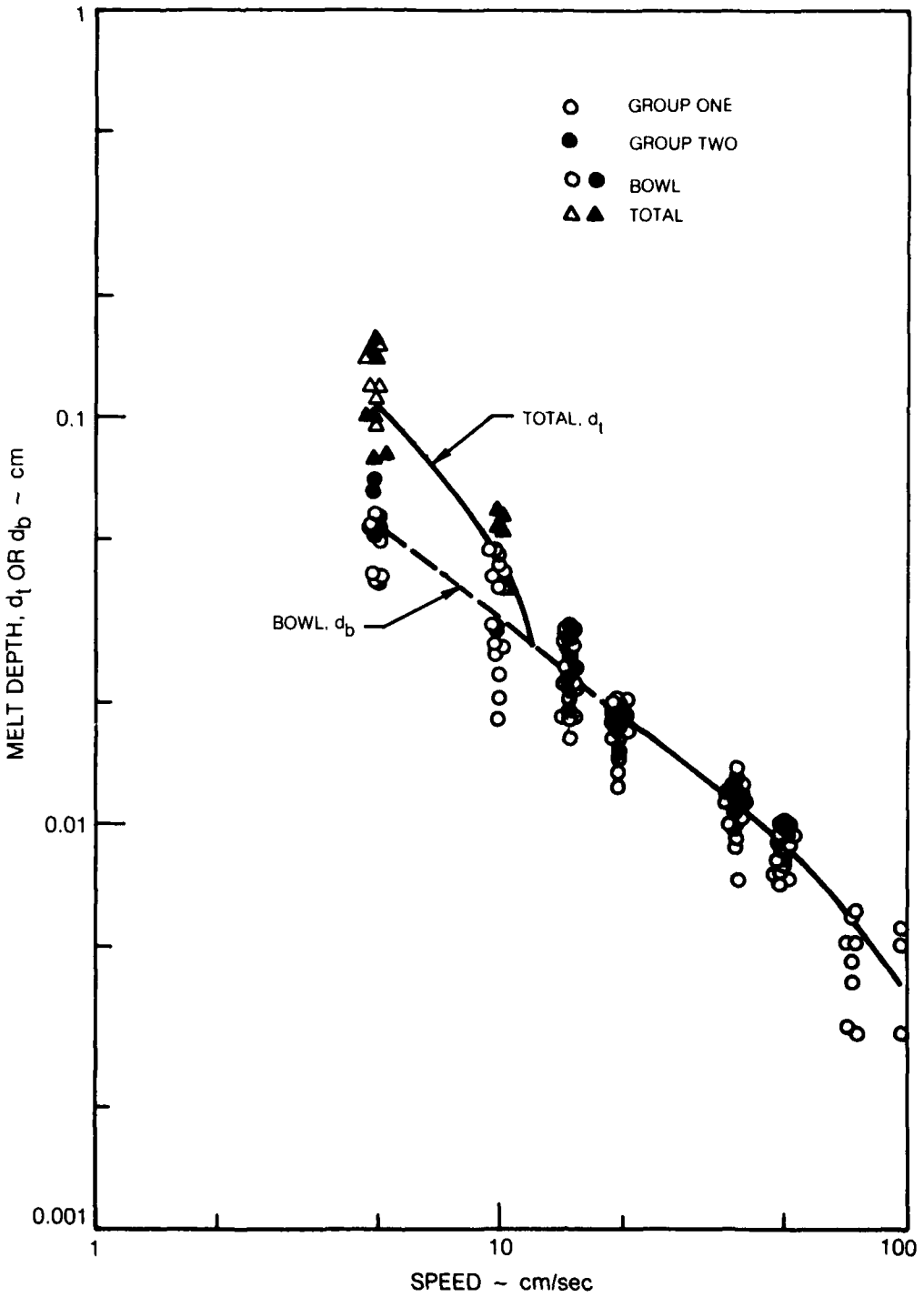

81-10-52-5

MELT DEPTH

4.70 kW

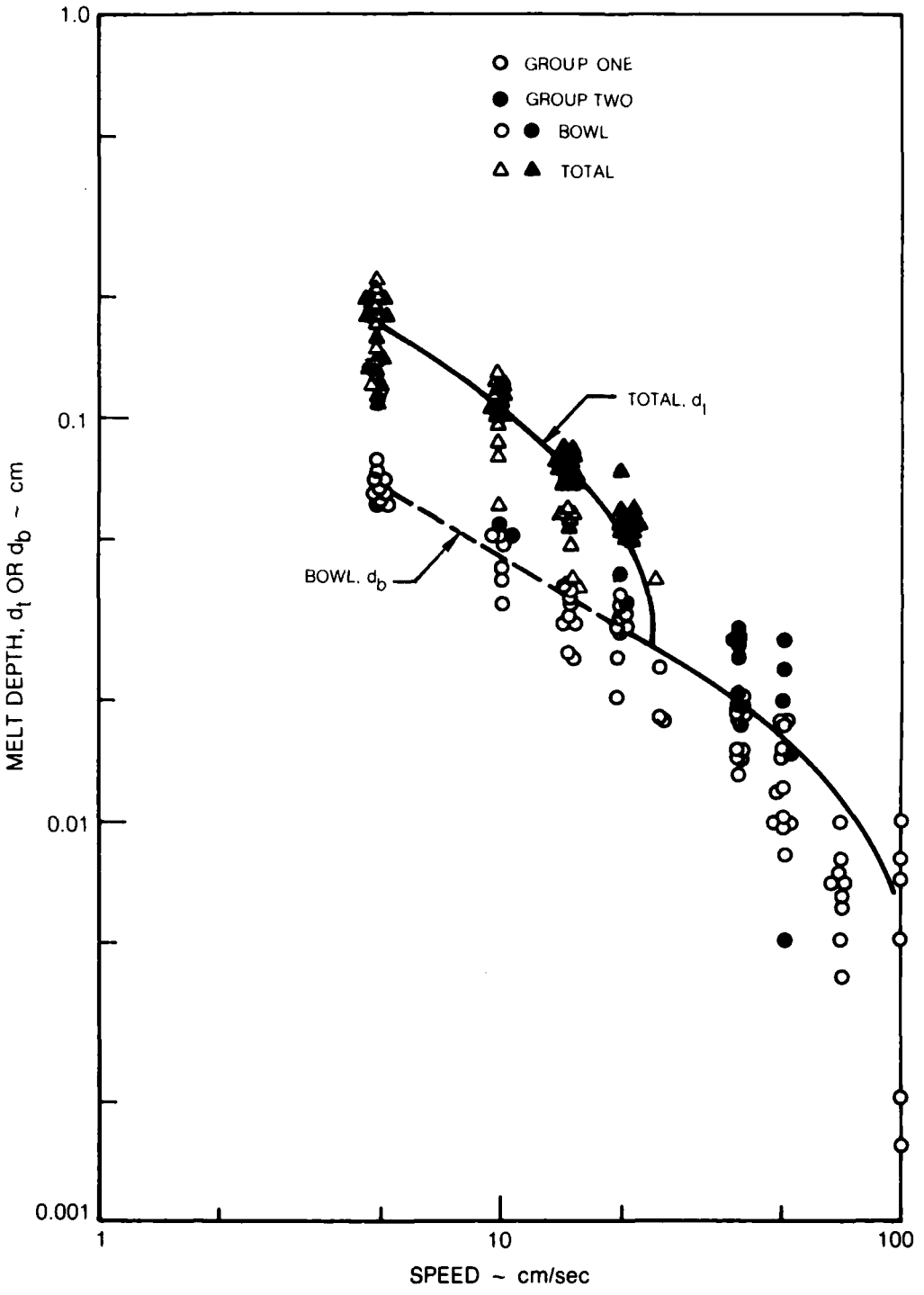

81-10-52-6

FIG. 8

MELT DEPTH

6.26 kW

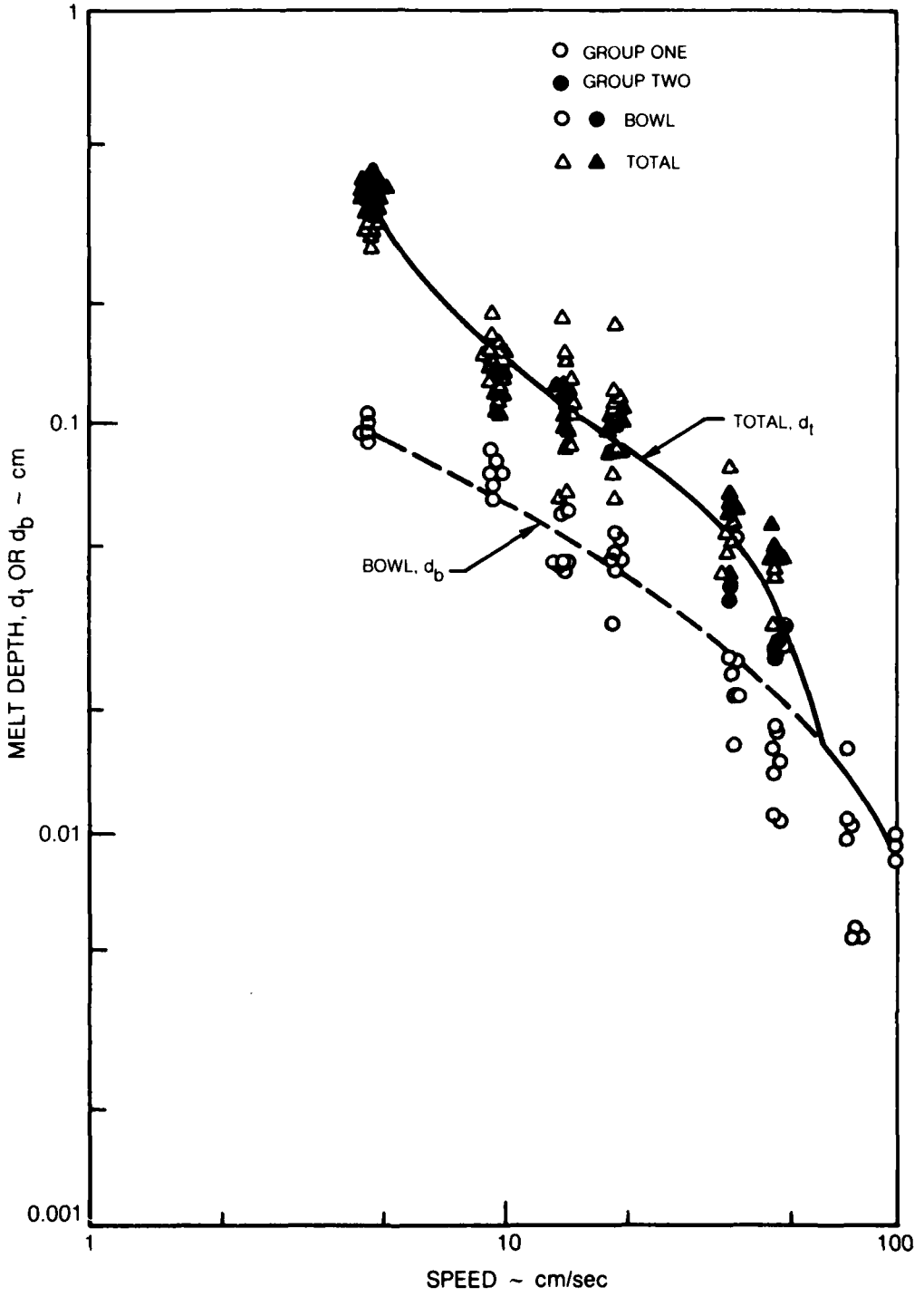

81-10-52-7

MELT DEPTH

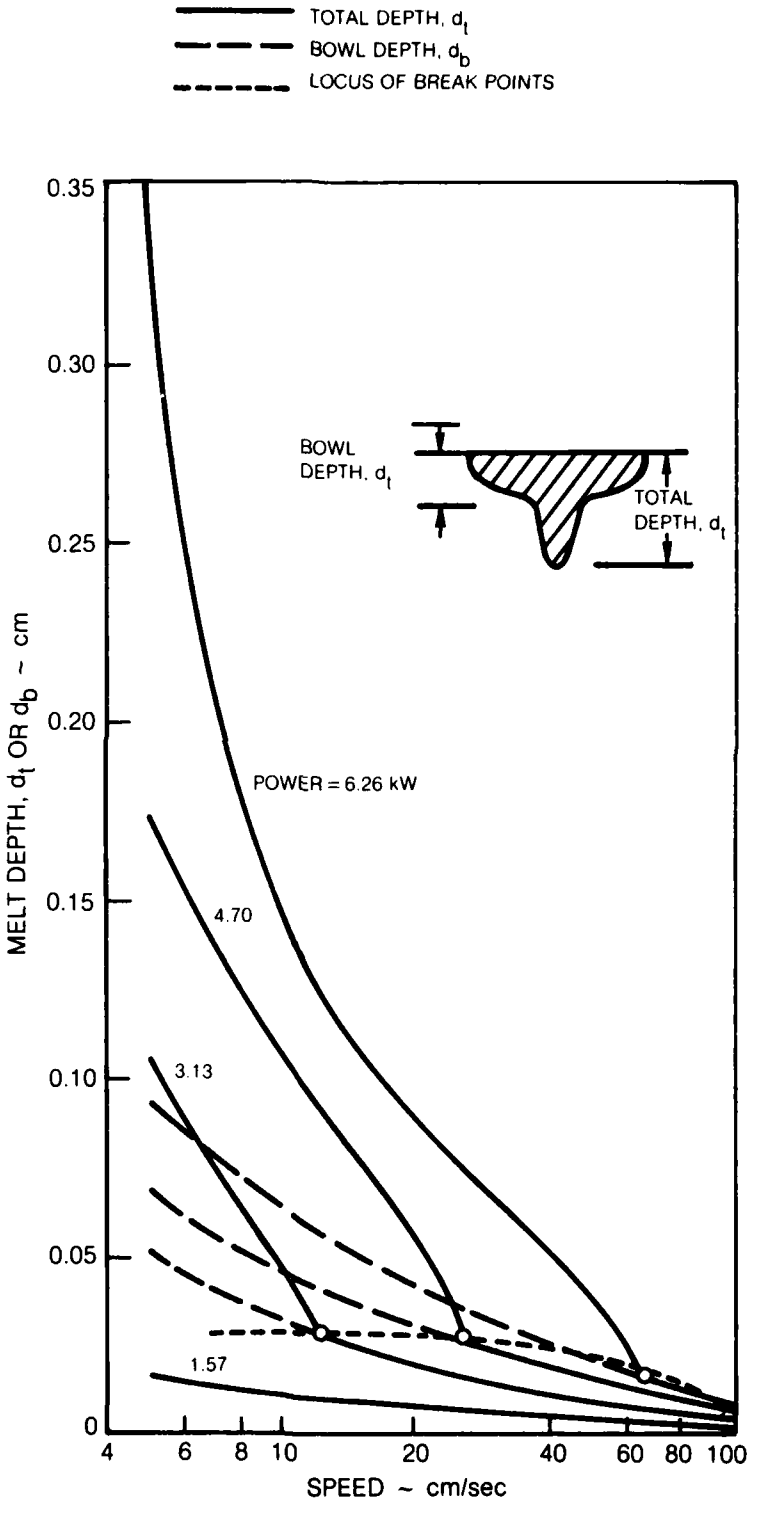

81-10-52-8

MELT WIDTH

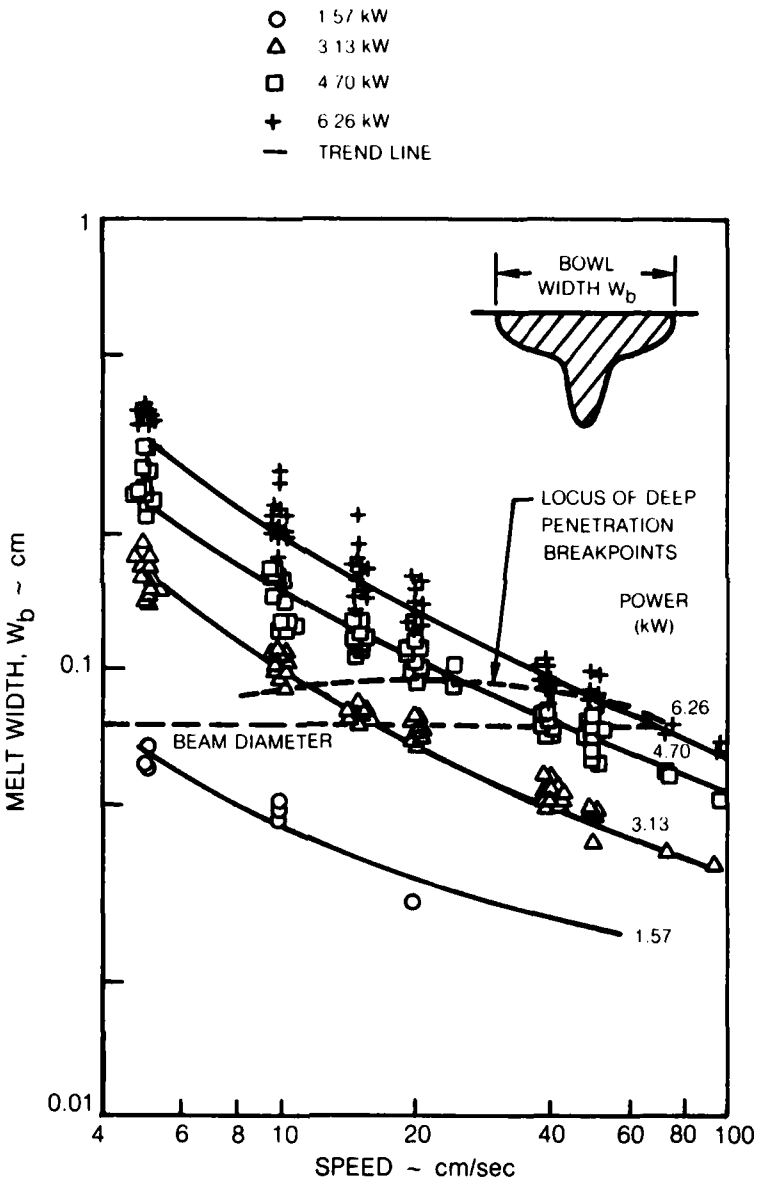

81-10-52-9

FIG. 11

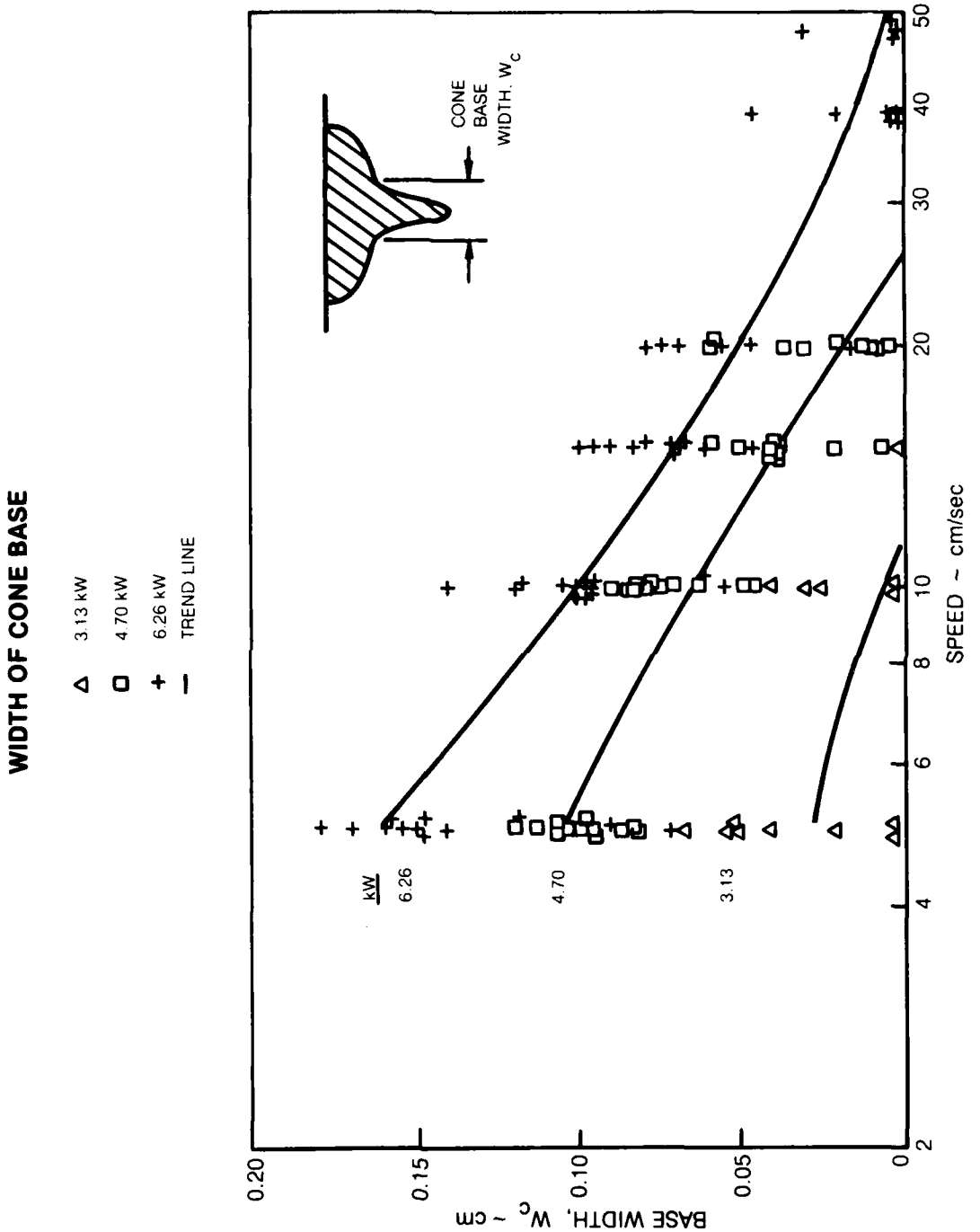

81-10-52-10

WELDING EFFICIENCY

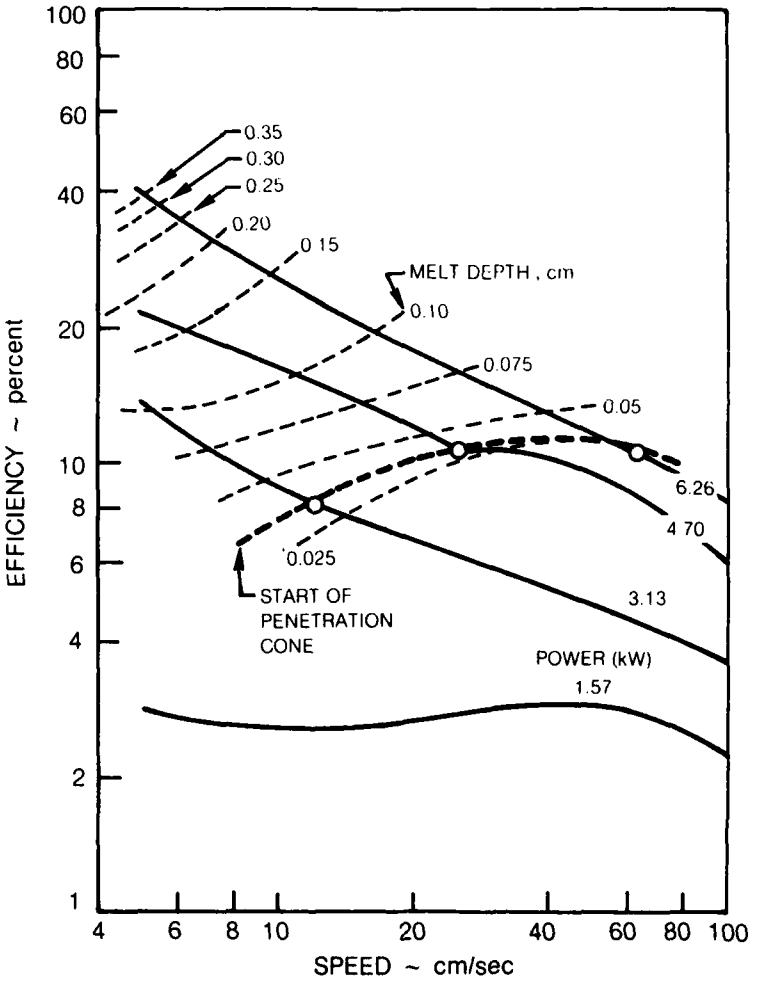

81-10-52-11

R82-914763-6

LONGITUDINAL SECTION, NEAR CENTERLINE OF FUSION ZONE OF 317L STAINLESS-CLAD STRUCTURAL HULL STEEL, ASTM A131

LASER WELDED AT 6.26 kW (AT WORKPIECE) BEAM POWER

5.1 cm/s BEAM TRAVERSE SPEED

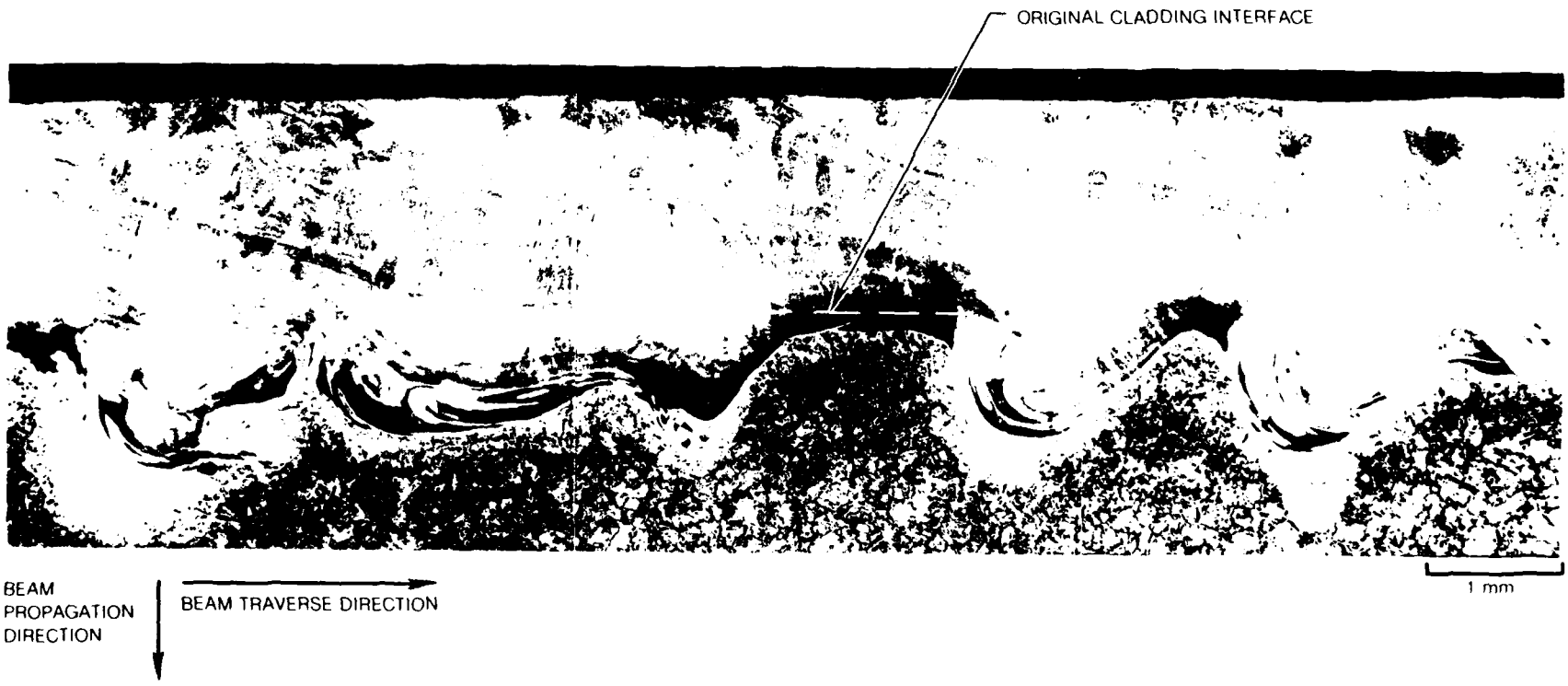

82-2-21-1

FIG. 13

FIG. 14

TRANSVERSE SECTION, CENTERLINE OF FUSION ZONE

POWER 6.36 kW AT SURFACE, BEAM TRAVERSE SPEED 5.1 cm/s

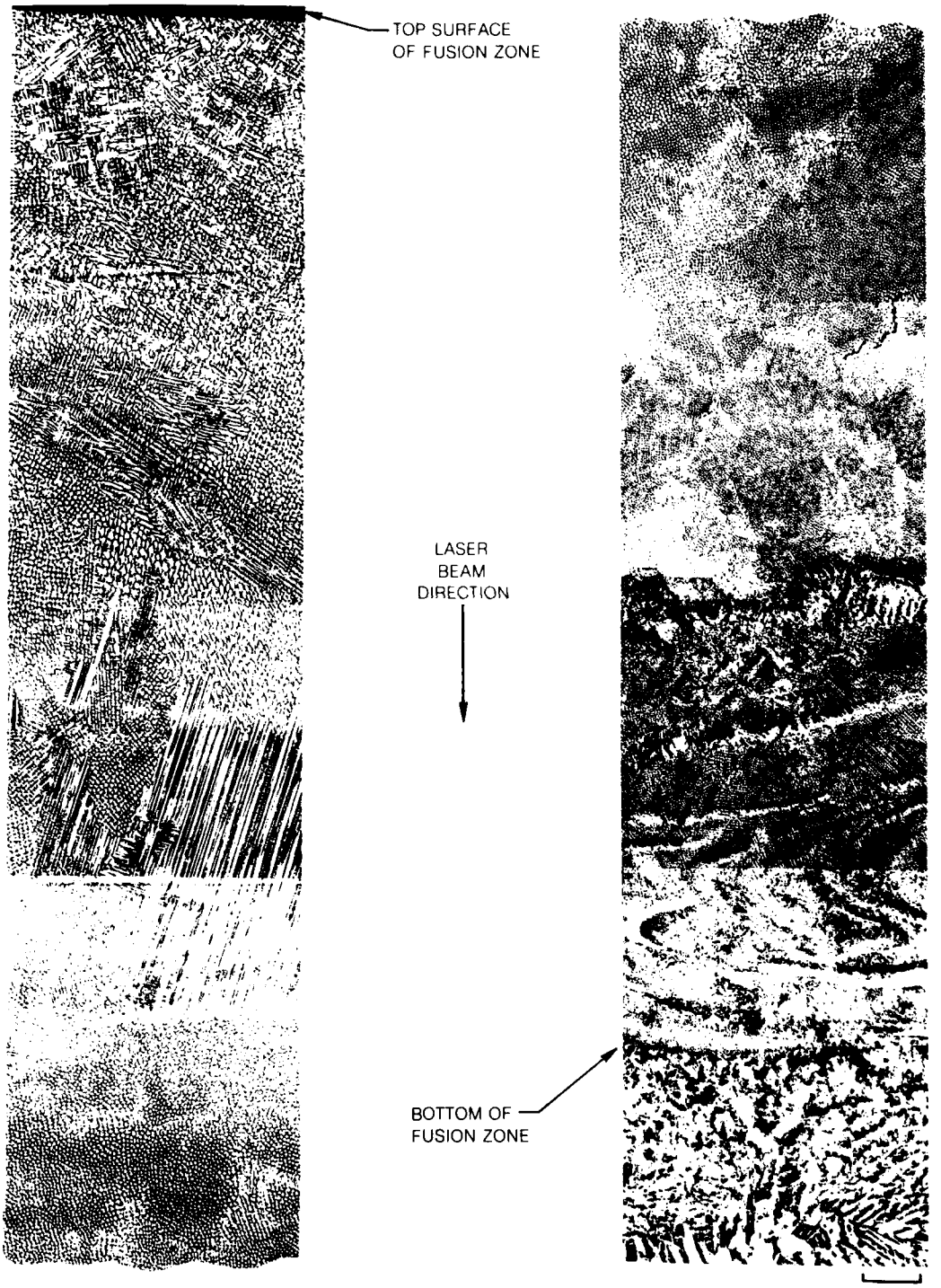

82-2-21-2

MICROSTRUCTURE OF FUSION ZONE, LASER WELD, 7.04 kW, 20.3 cm/s

7.04 kW DELIVERED POWER

20.3 cm/s TRAVERSE SPEED

CLADDING/SUBSTRATE INTERFACE

(a) LIGHT MICROGRAPH, TRANSVERSE SECTION
ORIGINAL CLADDING THICKNESS 1.4mm (0.055 in.)

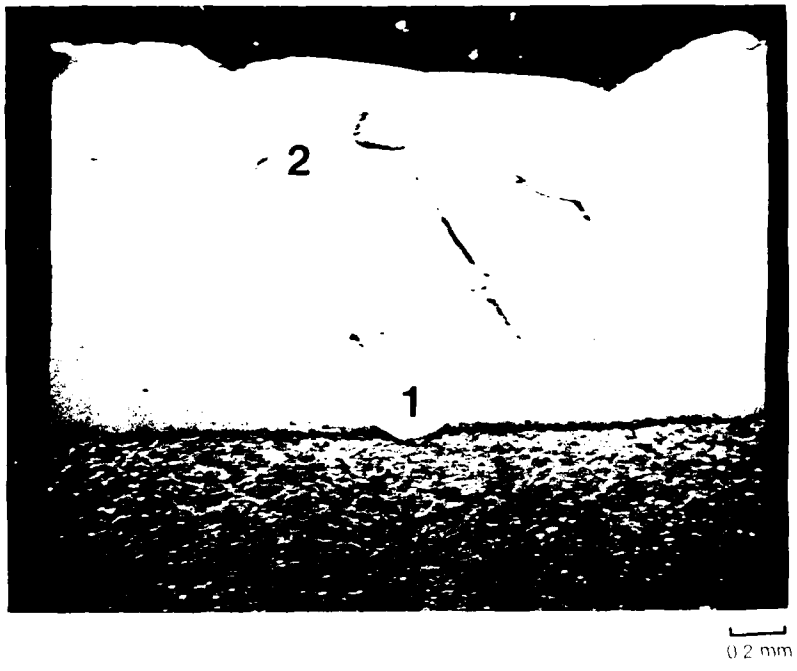

(b) SECONDARY ELECTRON IMAGE, TRANSVERSE SECTION
AREAS 1 AND 2 SHOWN IN FIGS. 16 AND 17

82-2-21-3

MICROSTRUCTURE AND DISTRIBUTION OF Cr, Ni, AND Fe, 7.04 kW, 20.3 cm/s

AREA 1 OF FUSION ZONE SHOWN IN FIG. 15(b) LASER WELDED AT 7.04 kW DELIVERED POWER AND 20.3 cm/s TRAVERSE SPEED

0.2 mm

(a) SECONDARY ELECTRON IMAGE, AREA 1, BOTTOM OF FUSION ZONE

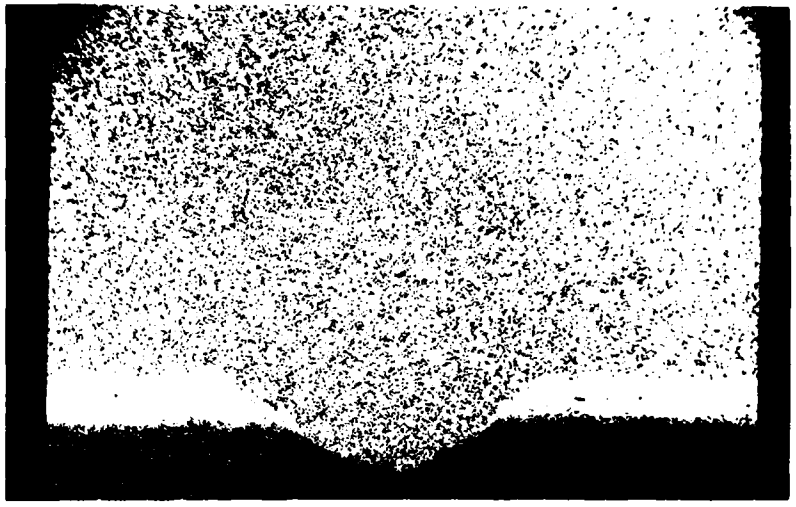

(c) NiKα SIGNAL: AREA OF (a)

Ni LAYER TO PROMOTE ROLL BONDING. CLADDING/SUBSTRATE INTERFACE

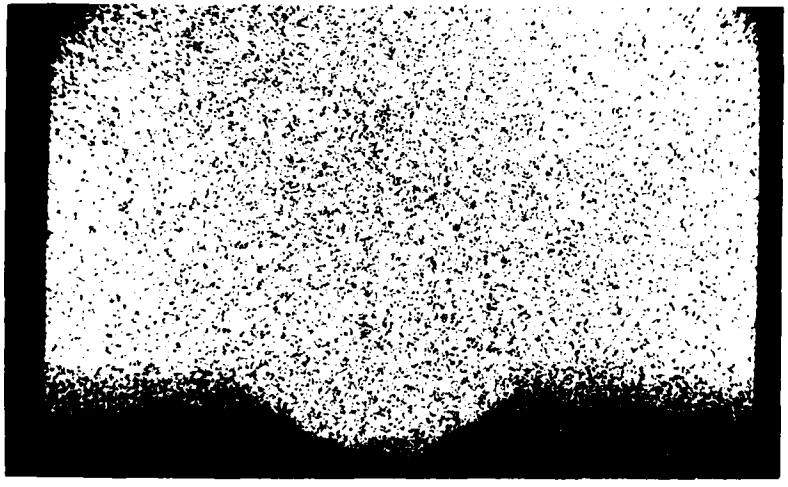

(b) CrKα SIGNAL, AREA OF (a), ABOVE

(d) FeKα SIGNAL, AREA OF (a)

82-2-21-4

R82-914763-6

FIG. 16

MICROSTRUCTURE AND DISTRIBUTION OF Cr, 7.04 kW, 20.3 cm/s

AREA 2 OF FUSION ZONE, LASER WELDED AT 7 04 kW DELIVERED POWER AND 20 3 cm/s TRAVERSE SPEED

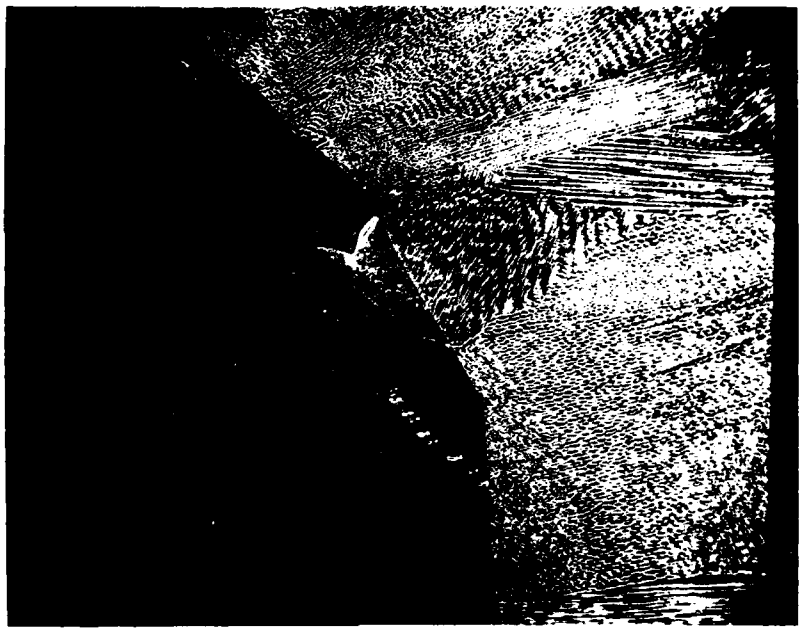

(a) SECONDARY ELECTRON IMAGE, AREA 2, SIDE OF FUSION ZONE

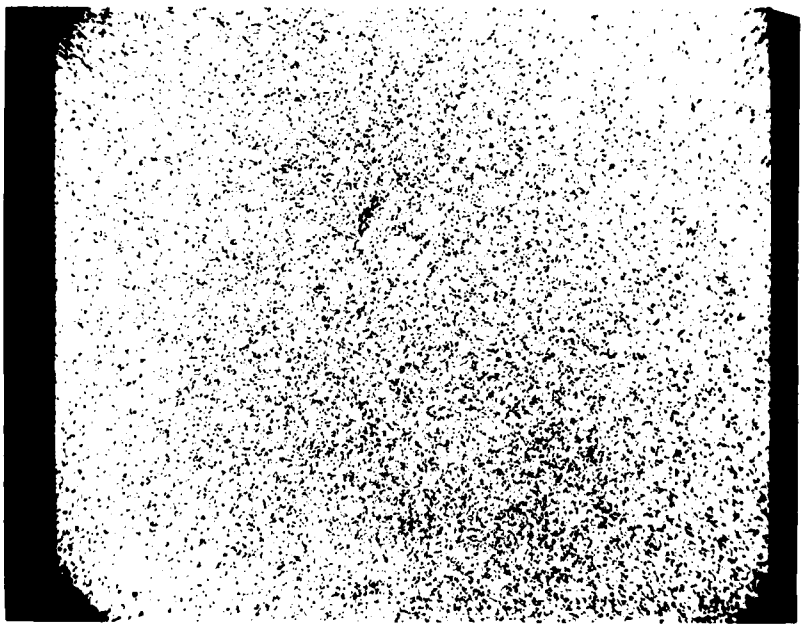

(b) CrKα SIGNAL, AREA OF (a), ABOVE

82-2-21-5

Cr AND Ni PROFILE PLOT

℄ OF FUSION ZONE SHOWN IN FIGURE 15. 7 04 kW. 20 3 cm/s

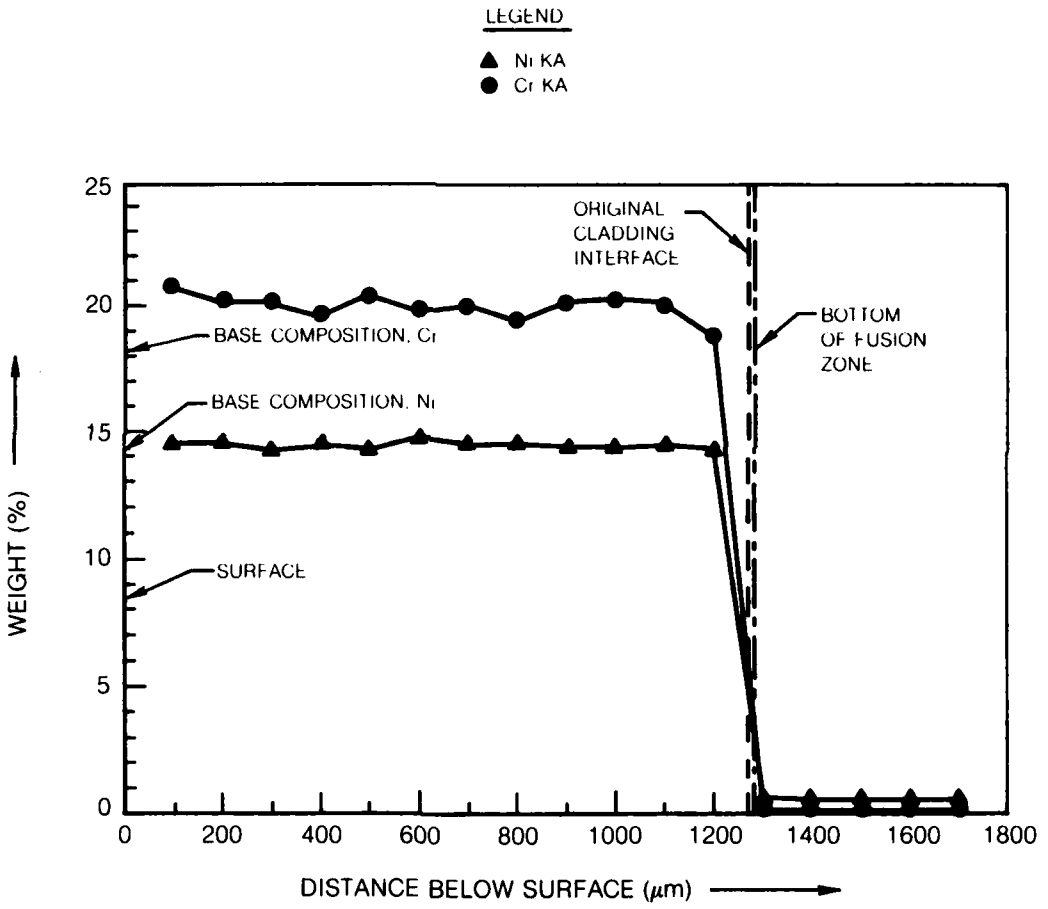

82-2-21-6

MICROSTRUCTURE OF FUSION ZONE, 6.26 kW, 5.1 cm/s

LASER WELD MADE AT 6.26 kW DELIVERED POWER AND 5.1 cm/s TRAVERSE SPEED

(a) LIGHT MICROGRAPH, TRANSVERSE SECTION
ORIGINAL CLADDING THICKNESS 2.03 mm (0.080 in.)

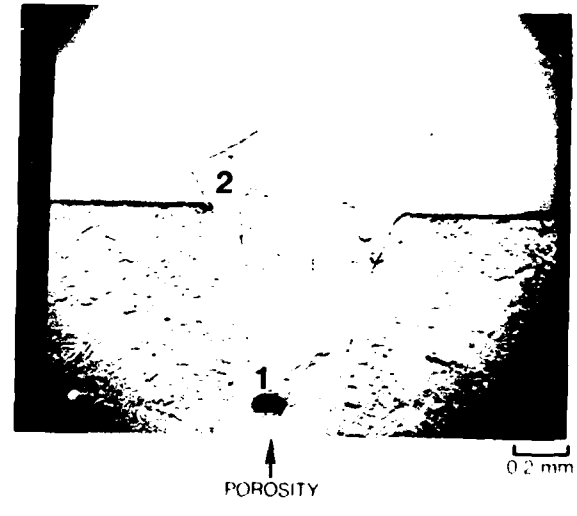

(b) SECONDARY ELECTRON IMAGE, TRANSVERSE SECTION
AREAS 1 AND 2 SHOWN IN FIGS. 20 AND 21

82-2-21-7

R82-914763-6

FIG. 19

FIG. 20

MICROSTRUCTURE AND DISTRIBUTION OF Cr AND Ni, 6.26 kW, 5.1 cm/s

AREA 1 OF FUSION ZONE SHOWN IN FIG. 19(b) LASER WELDED AT 6.26 kW DELIVERED POWER AND 5.1 cm/s TRAVERSE SPEED

(a) SECONDARY ELECTRON IMAGE, AREA 1

(b) CrKα SIGNAL, AREA OF (a)

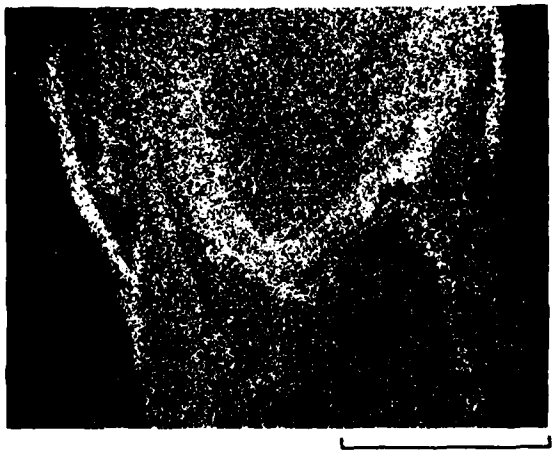

(c) NiKα SIGNAL, AREA OF (a)

82-2-21-8

MICROSTRUCTURE AND DISTRIBUTIONS OF Cr AND Ni, 6.26 kW, 5.1 cm/s

AREA 2 OF FUSION ZONE SHOWN IN FIG. 19(b) LASER WELDED AT 6.26 kW DELIVERED POWER AND 5.1 cm/s TRAVERSE SPEED

(a) SECONDARY ELECTRON IMAGE, AREA 2, SIDE OF FUSION ZONE

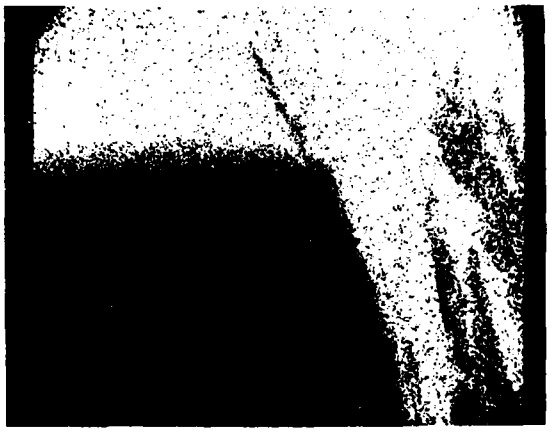

(b) CrKα SIGNAL, AREA OF (a)

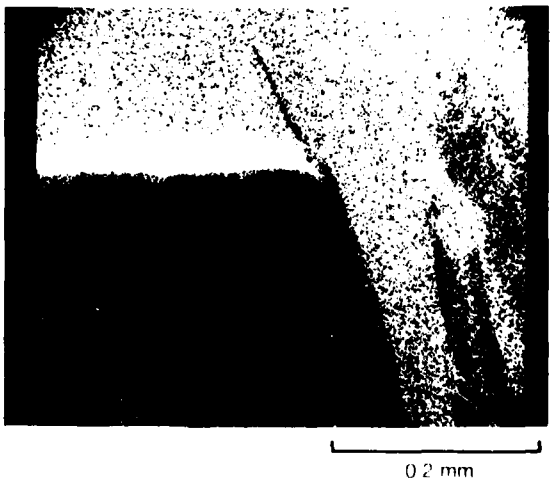

(c) NiKα SIGNAL AREA OF (a)

82-2-21-9

Cr AND Ni PROFILE PLOT

℄ OF FUSION ZONE, 6 26 kW, 5 1 cm/s

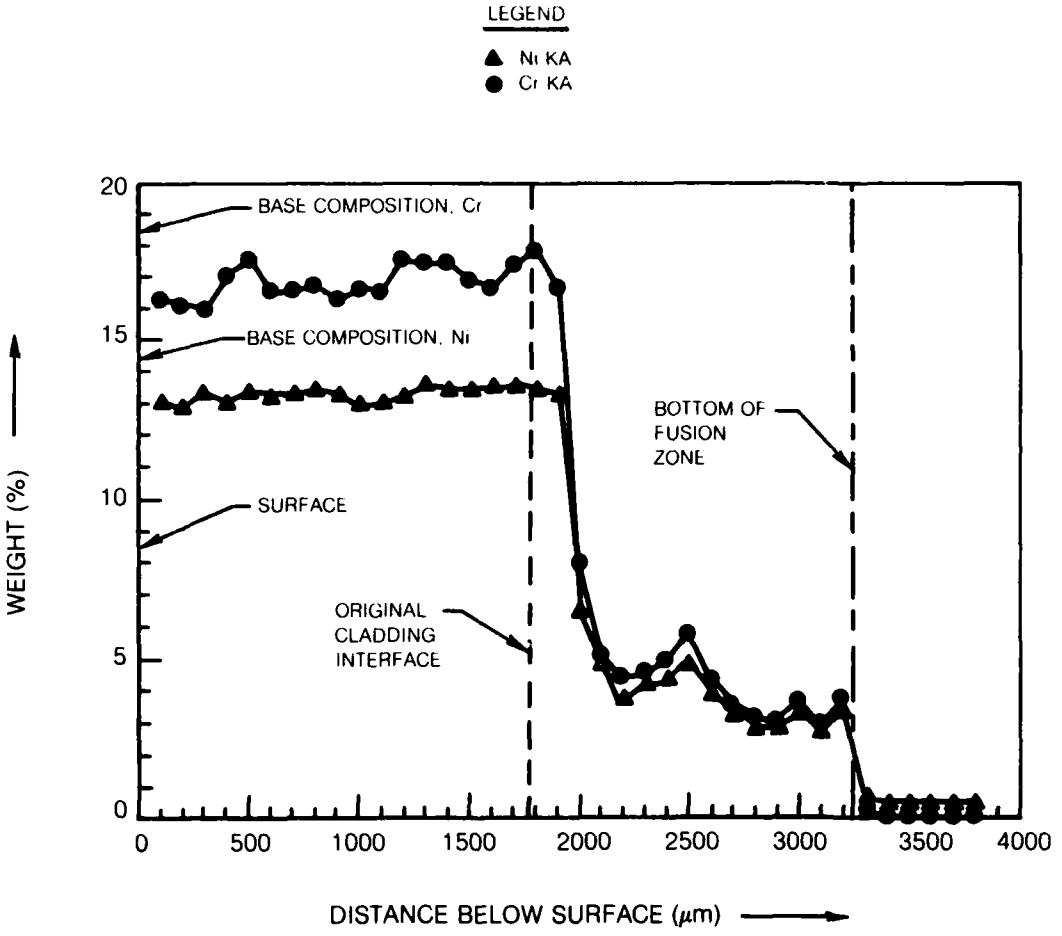

82-2-21-10

MICROSTRUCTURE OF FUSION ZONE, 6.26 kW, 5.1 cm/s

LASER WELD MADE AT 6.26 kW DELIVERED POWER AND 5.1 cm/s TRAVERSE SPEED

0.2 mm

LIGHT MICROGRAPH, TRANSVERSE SECTION.
ORIGINAL CLADDING THICKNESS 0.53mm (0.021 in.)

MICROSTRUCTURE OF FUSION ZONE, 6.26 kW, 5.1 cm/s

LASER WELD MADE AT 6.26 kW DELIVERED POWER AND 5.1 cm/s TRAVERSE SPEED

0.2 mm

SECONDARY ELECTRON IMAGE

82-2-21-12

R82-914763-6

FIG. 25

SECONDARY ELECTRON IMAGE OF ROOT OF FUSION ZONE, 6.26 kW, 5.1 cm/s

SHOWN IN FIG. 24. WELD MADE AT 6.26 kW AND 5.1 cm/s

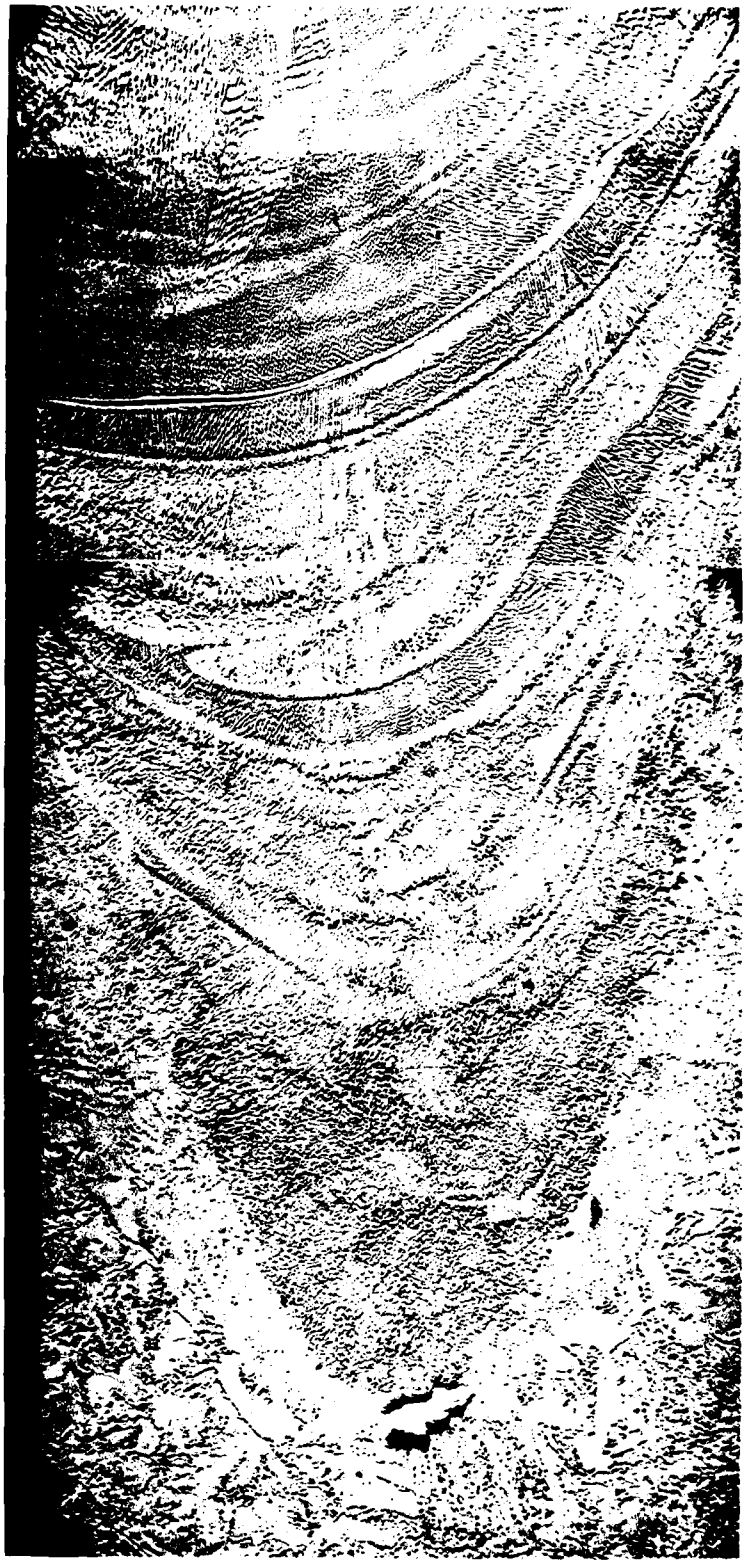

82-2-21-13

DISTRIBUTION OF Cr AND Ni, 6.26 kW, 5.1 cm/s

AREA AT ROOT OF FUSION ZONE SHOWN IN FIG. 25. WELD MADE AT 6.26 kW AND 5.1 cm/s

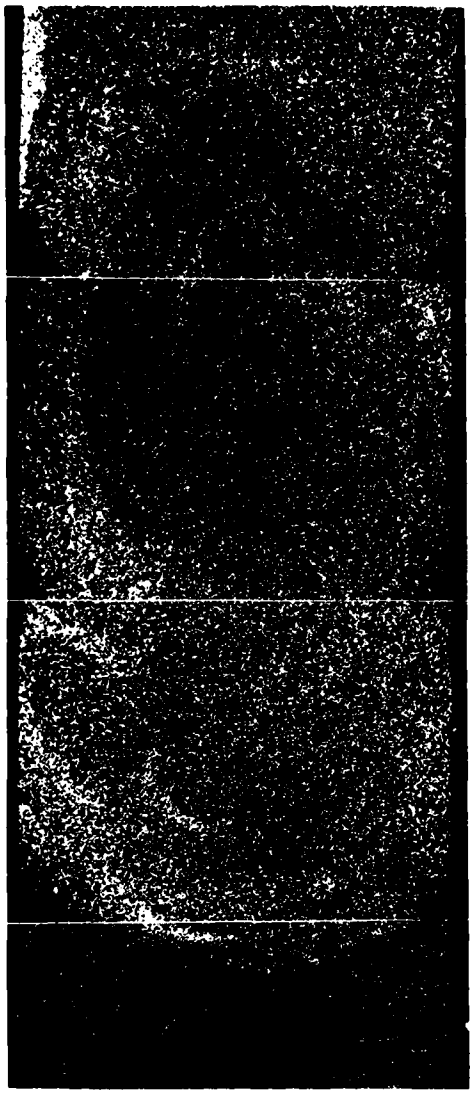

(a) CrKα SIGNAL

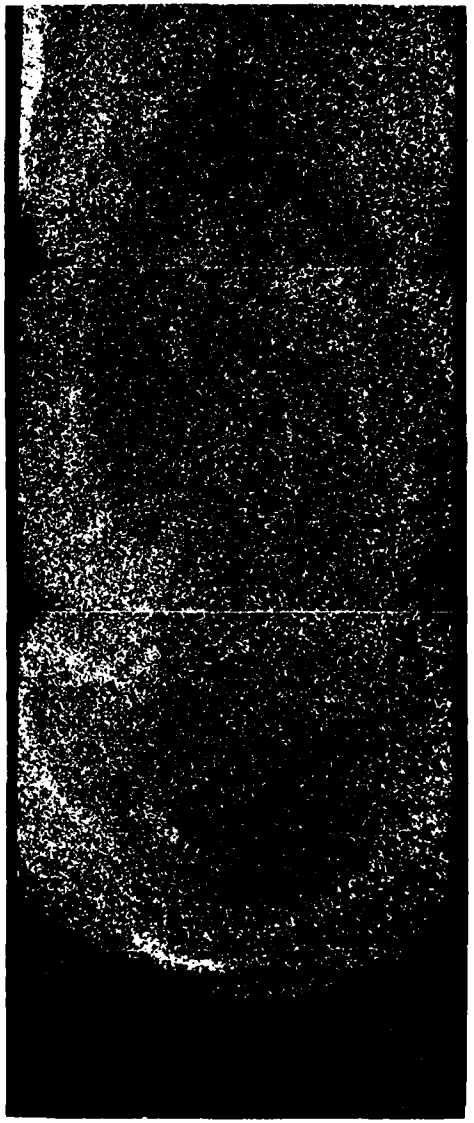

(b) NiKα SIGNAL

82-2-21-14

R82-914763-6

FIG. 26

Cr AND Ni PROFILE PLOT

℄ OF FUSION ZONE SHOWN IN FIG. 23, 6.26 kW, 5.1 cm/s

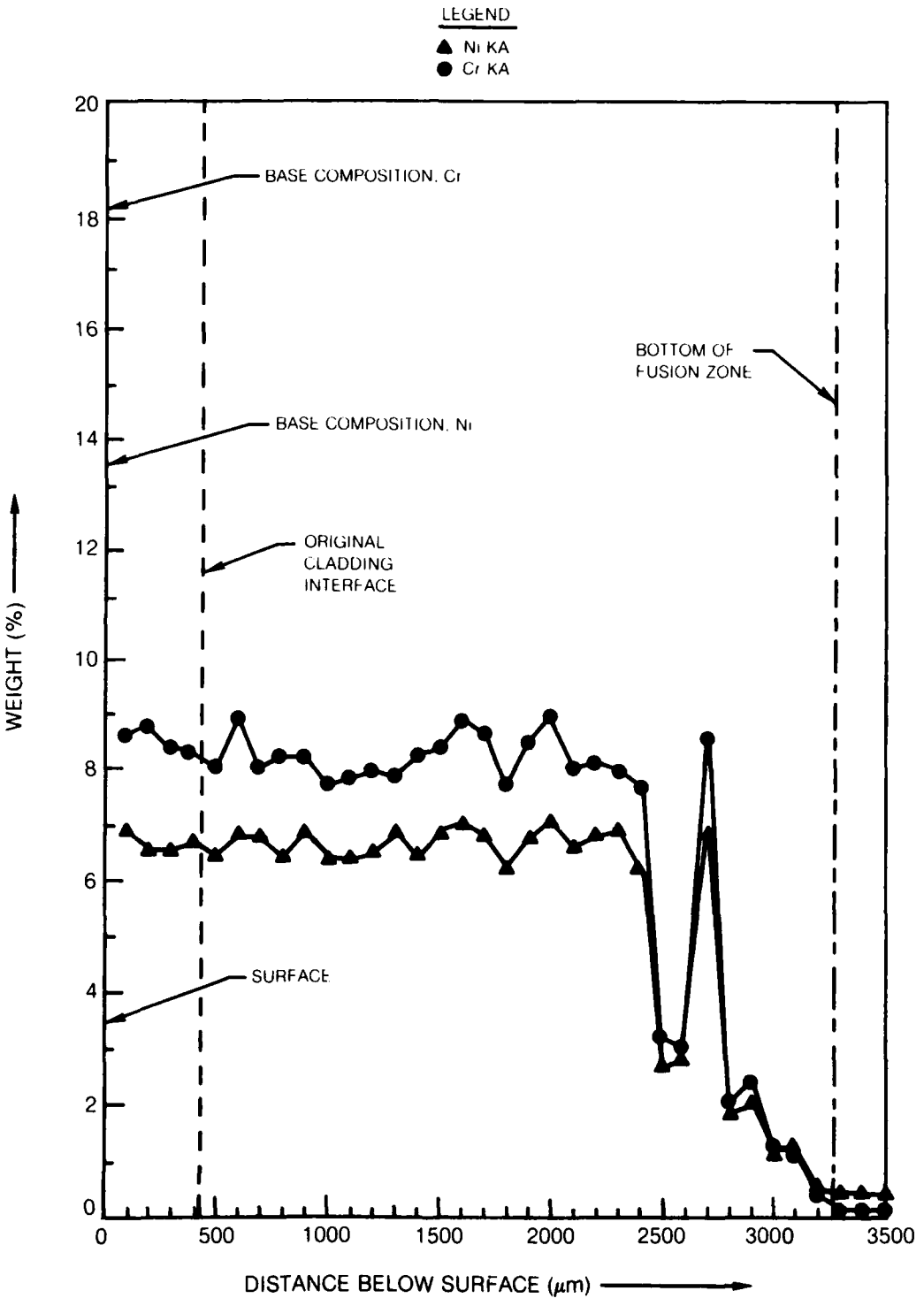

82-2-21-15

MICROSTRUCTURE OF FUSION ZONE, 7.04 kW, 5.1 cm/s

LASER WELD MADE AT 7.04 kW DELIVERED POWER AND 5 1 cm/s TRAVERSE SPEED

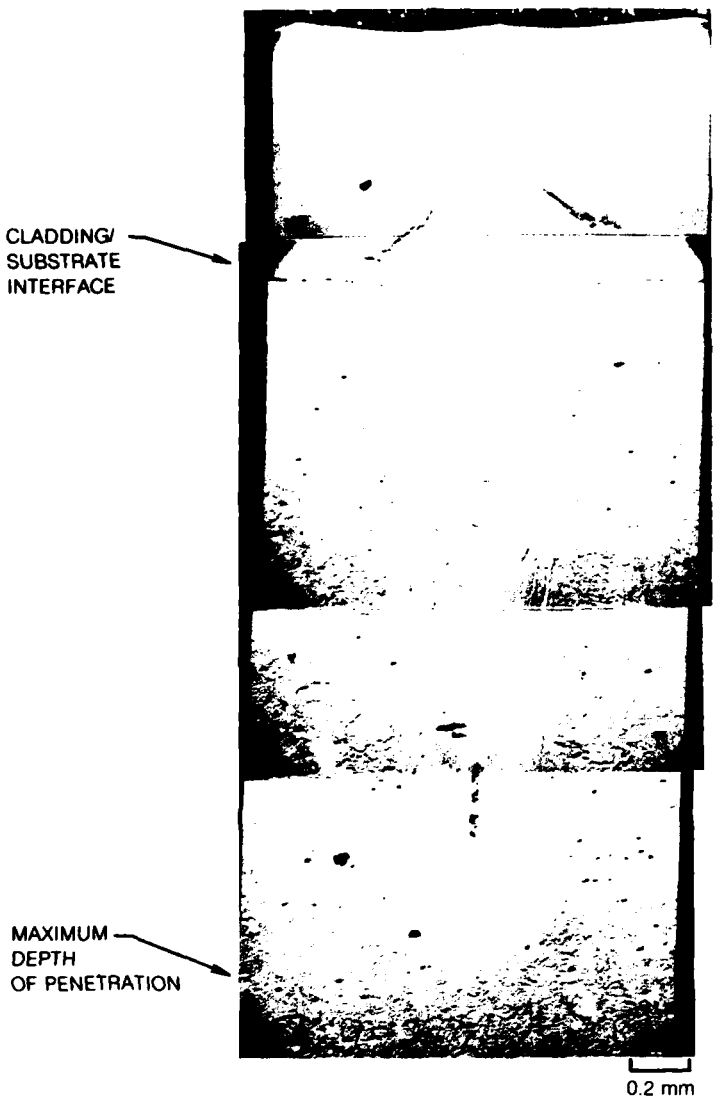

(a) SECONDARY ELECTRON IMAGE, ENTIRE FUSION ZONE

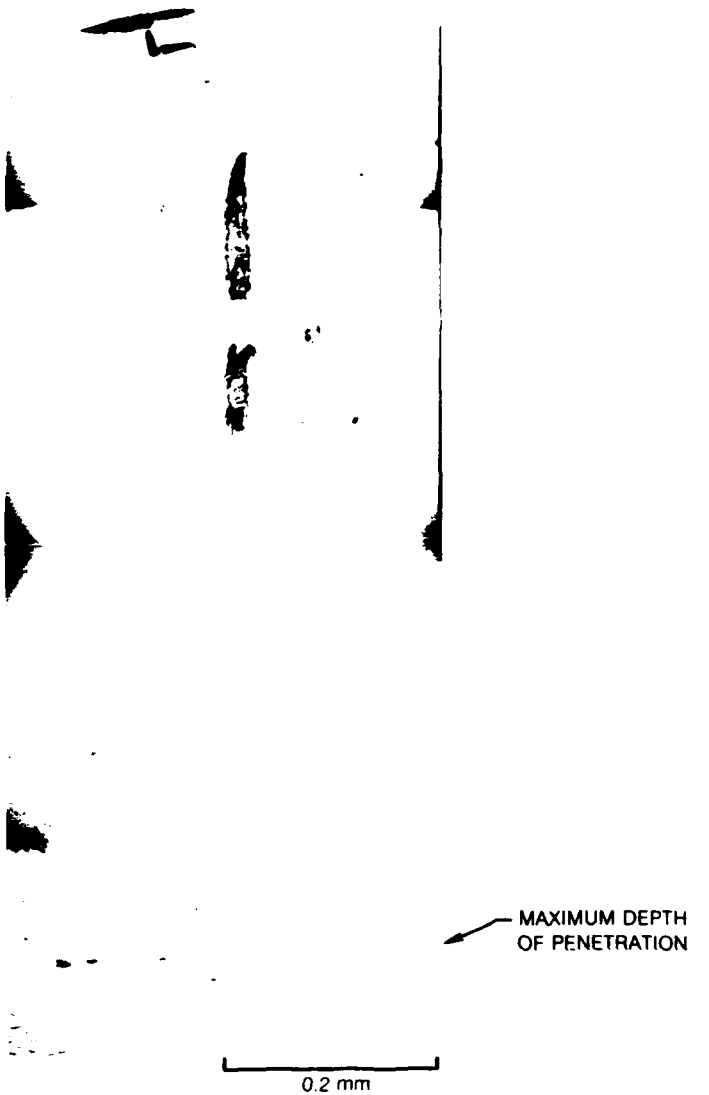

(b) SECONDARY ELECTRON IMAGE; ROOT OF FUSION ZONE

R82-914763-6

82-2-21-16

FIG. 28

DISTRIBUTION OF Cr AND Ni, 7.04 kW, 5.1 cm/s

AREA AT ROOT OF FUSION ZONE SHOWN IN FIG 28(b) WELD MADE AT 7 04 kW DELIVERED POWER AND 5 1 cm/s TRAVERSE SPEED

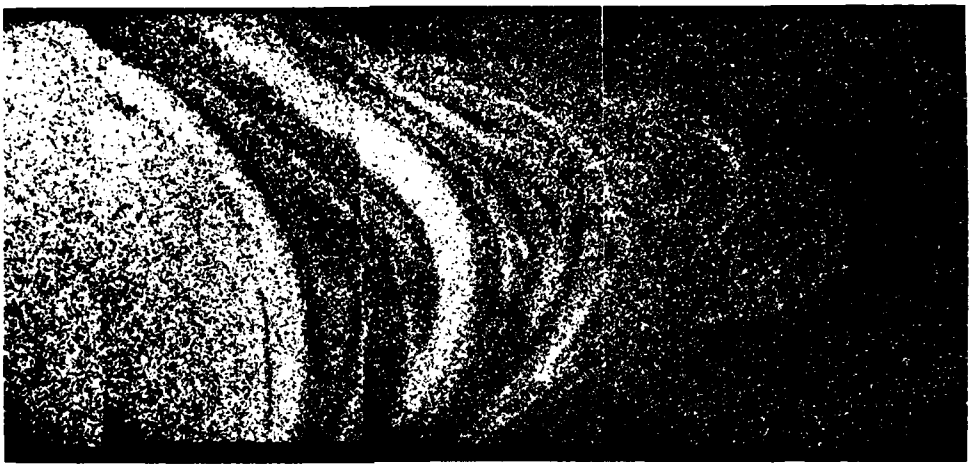

(b) NiKα SIGNAL

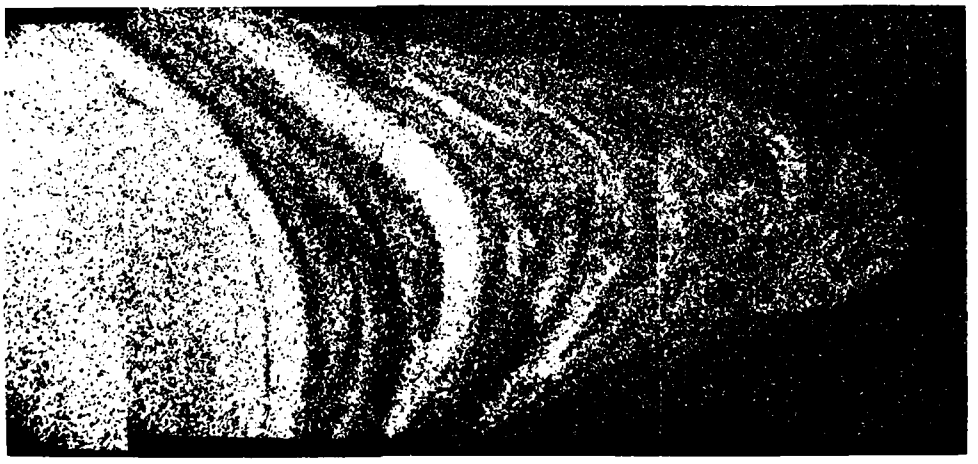

(a) CrKα SIGNAL

Cr AND Ni PROFILE PLOT

℄ OF FUSION ZONE, 7.04 kW, 5 cm/s

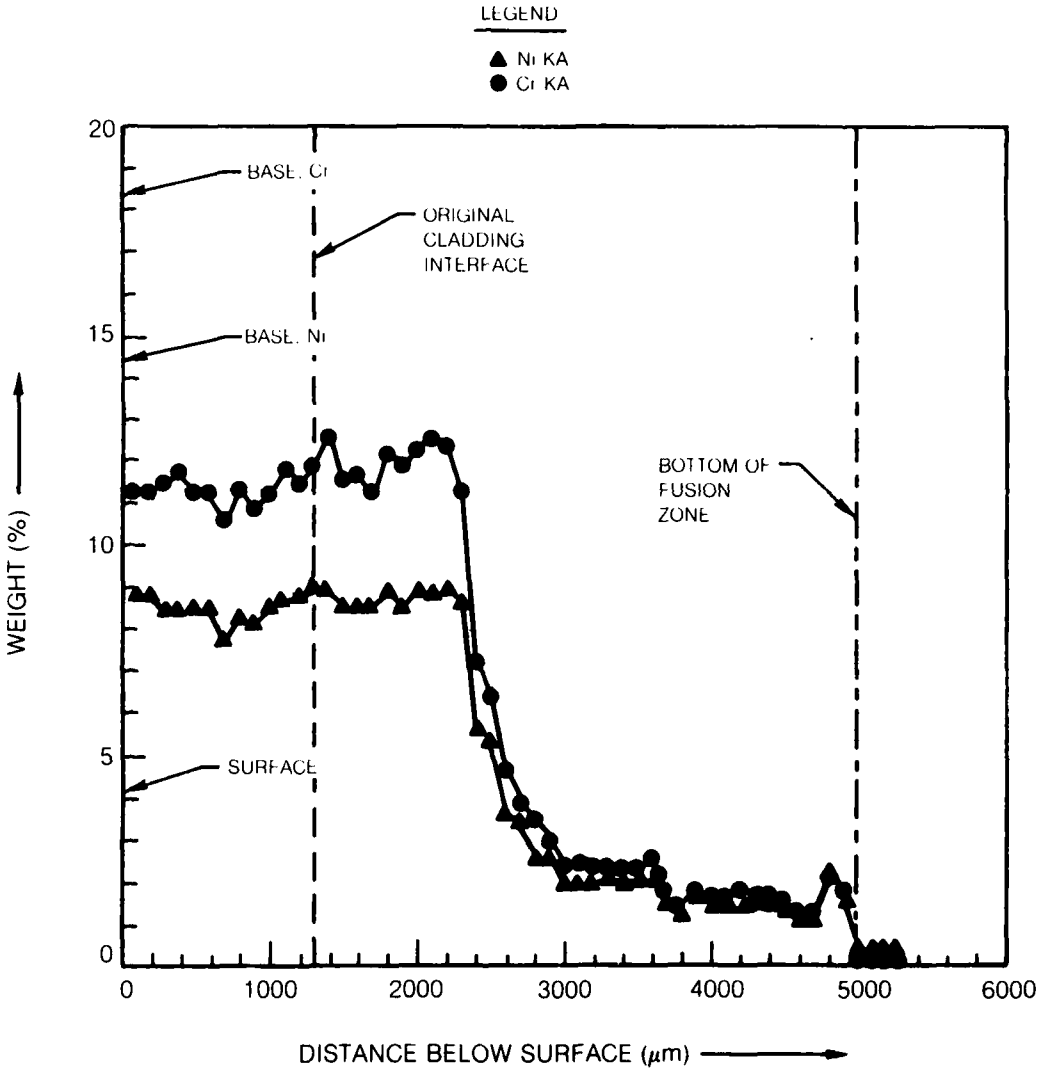

82-2-21-18

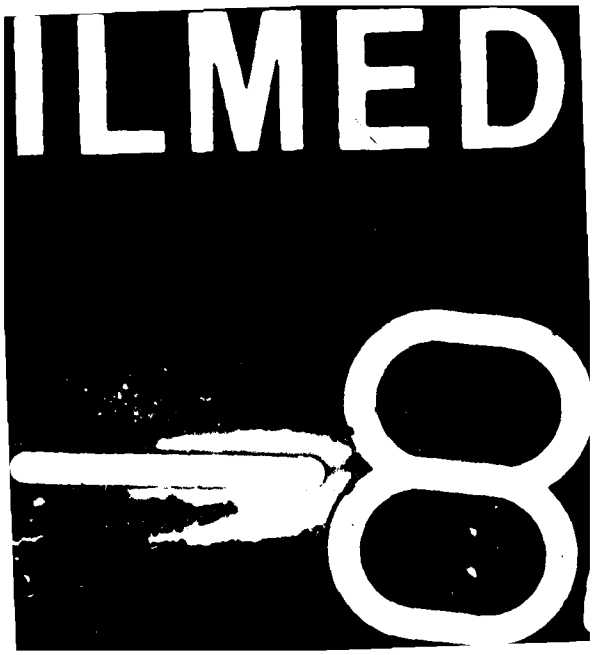
ILMED